

Received: 6 July 2012 – Accepted: 9 July 2012 – Published: 6 August 2012

Correspondence to: C. Hauri (chauri@alaska.edu)

Published by Copernicus Publications on behalf of the European Geosciences Union.

BGD

9, 10371–10428, 2012

**Variability and
long-term trends of
ocean acidification**

C. Hauri et al.

Title Page

Abstract

Introduction

Conclusions

References

Tables

Figures



Back

Close

Full Screen / Esc

Printer-friendly Version

Interactive Discussion



Abstract

Due to seasonal upwelling, the upper ocean waters of the California Current System (CCS) have a naturally low pH and aragonite saturation state (Ω_{arag}), making this region particularly prone to the effects of ocean acidification. Here, we use the Regional Oceanic Modeling System (ROMS) to conduct preindustrial and transient (1995–2050) simulations of ocean biogeochemistry in the CCS. The transient simulations were forced with increasing atmospheric $p\text{CO}_2$ as projected by the NCAR CSM 1.4 model run under either the IPCC SRES A2 or B1 scenarios. Using ROMS, we investigate the timing of transition decades during which pH and Ω_{arag} depart from their modeled preindustrial (1750) and present-day (2011) variability envelopes. We report these transition decades by noting the midpoint of the ten-year transition periods. In addition, we also analyze the timing of near permanent aragonite undersaturation in the upper 100 m of the water column. Our results show that an interplay of physical and biogeochemical processes create large seasonal variability in pH (~ 0.14) and Ω_{arag} (~ 0.2). Despite this large variability, we find that present-day pH and Ω_{arag} have already moved out of their preindustrial variability envelopes due to the rapidly increasing concentrations of atmospheric CO_2 . The simulations following the A2 emissions scenario suggest that nearshore surface pH of the northern and central CCS will move out of their present-day variability envelopes by 2045 and 2037, respectively. However, surface Ω_{arag} of the northern and central CCS subregions are projected to depart from their present-day variability envelopes sooner, by 2030 and 2035, respectively. By 2025, the aragonite saturation horizon of the central CCS is projected to shoal into the upper 75 m for the duration of the annual cycle, causing near permanent undersaturation in subsurface waters. Overall, our study shows that the CCS joins the Arctic and Southern Oceans as one of only a few known ocean regions presently approaching this dual threshold of undersaturation with respect to aragonite and a departure from its variability envelope. In these regions, organisms may be forced to rapidly adjust to conditions that are both inherently chemically challenging and also substantially different from prior conditions.

Variability and long-term trends of ocean acidification

C. Hauri et al.

Title Page

Abstract

Introduction

Conclusions

References

Tables

Figures



Back

Close

Full Screen / Esc

Printer-friendly Version

Interactive Discussion



1 Introduction

Since the onset of the industrial era, the oceans have absorbed about one third of the anthropogenically emitted carbon dioxide (Sabine et al., 2004). The uptake of anthropogenic CO₂ by the oceans has already reduced the global surface ocean pH by about 0.1 units (Feely et al., 2004) and it is projected to decrease another 0.3 to 0.4 pH units by the end of this century under the IPCC 1992 (IS92a) scenario (788 ppm in 2100, Orr et al., 2005). This chemical change, known as ocean acidification, leads also to a decline in the saturation state (Ω) of seawater with respect to calcium carbonate minerals, such as calcite or the less stable form aragonite. While this altered carbon chemistry and its effects on marine ecosystems are an ongoing subject of intensive scientific research (Doney et al., 2012), early results have demonstrated that these changes can have deleterious effects on marine calcifying invertebrates such as corals, coralline algae, oyster larvae and pteropods (Orr et al., 2005; Kleypas et al., 2006; Martin and Gattuso, 2009).

The California Current System (CCS) has a naturally low pH and aragonite saturation state (Ω_{arag}), making it particularly prone to the effects of ocean acidification (Feely et al., 2008; Gruber et al., 2012). Seasonal upwelling is induced by equator-ward winds in early spring. The upwelling brings cold subsurface water, rich in nutrients and dissolved inorganic carbon (DIC), up to the surface and triggers a series of biological processes. The high DIC content of the upwelled waters endows them with a low pH and Ω_{arag} . Once close to the surface, the nutrient-rich water triggers phytoplankton blooms that then draw down oceanic $p\text{CO}_2$ to levels sometimes below atmospheric $p\text{CO}_2$ (Hales et al., 2005), causing an increase in surface water pH and Ω_{arag} . Conversely, remineralization processes of sinking organic matter counteract the effects of production by lowering pH and Ω_{arag} . Physical circulation can affect the duration and magnitude of these biological processes and therefore plays a role in controlling the evolution and spatial pattern of pH and Ω_{arag} .

BGD

9, 10371–10428, 2012

Variability and long-term trends of ocean acidification

C. Hauri et al.

Title Page

Abstract

Introduction

Conclusions

References

Tables

Figures

◀

▶

◀

▶

Back

Close

Full Screen / Esc

Printer-friendly Version

Interactive Discussion



The strong physical and biological dynamics of the CCS create large spatial and temporal variability in pH and Ω_{arag} (Feely et al., 2008; Juranek et al., 2009; Alin et al., 2012). North of Point Conception (34.5° N), a combination of strong seasonal upwelling events and remineralization trigger a pH drop to 7.65 and Ω_{arag} to 0.8 at the surface in some nearshore environments (Feely et al., 2008). Combined with adjacent high biological production, a heterogeneous distribution of pH and Ω_{arag} is created. Offshore pH and Ω_{arag} are not directly influenced by upwelling and remain above 8.0 and 2.2, respectively. Reconstructed pH and Ω_{arag} from temperature (T) and oxygen (O_2) time-series from the Central Oregon shelf display a seasonal range of Ω_{arag} of 0.8–1.8 at 30 m (Juranek et al., 2009), with lowest levels during the upwelling season between spring and fall. South of Point Conception, upwelling-favorable winds are weaker, yet more persistent throughout the year (Dorman and Winant, 1995). In contrast to the area north of Point Conception, reconstructed pH and Ω_{arag} from T and O_2 time-series display highest levels in summer, due to biological drawdown of CO_2 in warm subsurface waters (30 m). Spatial variability is also highest in summer, most likely driven by an interplay of high productivity and upwelling, conveying DIC-rich water to the surface (Alin et al., 2012). At the Santa Monica Bay Observatory (SMBO at 33°55.9' N and 118°42.9' W), surface pH and Ω_{arag} display a large seasonal variability, ranging by ± 0.08 (1 STD) and ± 0.4 , respectively (Leinweber and Gruber, 2012).

The aragonite saturation horizon has shoaled 50–100 m since the preindustrial era (Feely et al., 2008; Hauri et al., 2009; Juranek et al., 2009) and will continue to rise in response to future oceanic uptake of anthropogenic CO_2 . Simulations forced with increasing atmospheric pCO_2 as projected by the NCAR CSM 1.4 model run under the IPCC SRES A2-scenario (Nakićenović and Swart, 2000) suggest that about 70 % of the euphotic nearshore region of the Central US West Coast become undersaturated with regard to aragonite ($\Omega < 1$) during the upwelling season by 2050, while within the next 20 to 30 yr this “absolute” threshold of aragonite undersaturation will be reached throughout the year in nearly all habitats along the seafloor (Gruber et al., 2012).

Variability and long-term trends of ocean acidification

C. Hauri et al.

[Title Page](#)[Abstract](#)[Introduction](#)[Conclusions](#)[References](#)[Tables](#)[Figures](#)[⏪](#)[⏩](#)[◀](#)[▶](#)[Back](#)[Close](#)[Full Screen / Esc](#)[Printer-friendly Version](#)[Interactive Discussion](#)

**Variability and
long-term trends of
ocean acidification**

C. Hauri et al.

Title Page

Abstract

Introduction

Conclusions

References

Tables

Figures

◀

▶

◀

▶

Back

Close

Full Screen / Esc

Printer-friendly Version

Interactive Discussion



Due to the large natural variability of pH and Ω_{arag} , it is possible that the organisms of the CCS are successfully adjusted to such extreme levels of pH and Ω_{arag} . Therefore, in order to evaluate the regional impact of ocean acidification, it is also necessary to define a “relative” threshold by comparing future trajectories of pH and Ω_{arag} to the current and prior conditions. Eventually the anthropogenic trend of ocean acidification will drive the waters towards levels of pH and Ω_{arag} that are outside the preindustrial or present-day variability envelope, suggesting that organisms will no longer be living under the same conditions once experienced. After these transition periods, we expect that the altered chemical environment will stress some organisms and have the potential to modify species viability and ecosystem structure. Cooley et al. (2012) and Friedrich et al. (2012) have used Earth System Models to study this relative threshold on a regional basis. However, the coarsely resolved global models don't resolve local dynamics, such as coastal upwelling, which in turn leads to an overestimation of pH and Ω_{arag} levels and underestimation of their temporal and spatial variability.

Here, we use the 5 km resolution, three dimensional physical circulation model ROMS (Regional Ocean Modeling System) coupled to a simple nitrogen based NPZD (Nutrient – Phytoplankton – Zooplankton – Detritus) model (Gruber et al., 2006) to describe the spatiotemporal variability of pH and Ω_{arag} in the CCS from the Mexican to the Canadian border, project future trajectories and identify the timing when pH and Ω_{arag} move out of their modeled variability envelopes. We will investigate whether the CCS, despite its high variability, is projected to approach the combined absolute and relative thresholds of both chemical dissolution of aragonite and a departure from the variability envelopes of pH and Ω_{arag} .

2 Methods

2.1 Model setup

We used a United States West Coast configuration of the three-dimensional physical ocean circulation model ROMS (Marchesiello et al., 2003; Shchepetkin and McWilliams, 2005), which simulates flow and mixing of ocean waters at an eddy-resolving horizontal resolution of 5 km. The model covers a 1300 km wide section along the US West Coast from the US/Canadian border past the US/Mexican border to 30° N (Fig. 1). The model grid is defined by horizontal curvilinear coordinates and a terrain-following vertical coordinate (σ) with 32 depth levels, with enhanced resolution near the surface and nearshore on the shallow shelf (see Gruber et al., 2011; Lachkar and Gruber, 2011, for a detailed description of the model setup).

The biogeochemical model used here is a simple nitrogen-based NPZD₂ and is described in detail in Gruber et al. (2006). The analyzed simulations are identical to the ones presented in Gruber et al. (2012) and are based on the same ecological parameters as used in Lachkar and Gruber (2011). The model system consists of nitrate (NO_3^-) and regenerated nitrogen (NH_4^+) pools, phytoplankton, zooplankton and two detritus pools. The large detritus pool sinks fast (10 m day^{-1}) and the smaller one sinks at a slower rate (1 m day^{-1}). However, the small detritus pool coagulates with phytoplankton to form large detritus, which increases its sinking speed. The carbon fluxes are tied to those of nitrogen with a fixed stoichiometric ratio of 106 : 16 (Redfield et al., 1963). DIC, Alkalinity (Alk) and CaCO_3 are part of the pool of biogeochemical state variables. DIC concentrations are dependent on gas exchange, CaCO_3 precipitation and dissolution and the net community production, which consists of the net primary production minus heterotrophic respiration. The Alk level is affected by the formation of NO_3^- (Nitrification) and removal of NO_3^- (new production) and also the precipitation and dissolution of CaCO_3 . The biogenic CaCO_3 formation is parameterized as 7% of the net primary production, such that for each mole of organic carbon formed by

BGD

9, 10371–10428, 2012

Variability and long-term trends of ocean acidification

C. Hauri et al.

Title Page

Abstract

Introduction

Conclusions

References

Tables

Figures

◀

▶

◀

▶

Back

Close

Full Screen / Esc

Printer-friendly Version

Interactive Discussion



**Variability and
long-term trends of
ocean acidification**

C. Hauri et al.

Title Page

Abstract

Introduction

Conclusions

References

Tables

Figures

◀

▶

◀

▶

Back

Close

Full Screen / Esc

Printer-friendly Version

Interactive Discussion



NPP, 0.07 mol of CaCO_3 are formed. CaCO_3 dissolves at a fixed dissolution rate of 0.0057 day^{-1} and sinks at a velocity of 20 m day^{-1} , which is twice the large detritus sinking velocity. Oceanic $p\text{CO}_2$ is calculated from DIC, Alk, temperature (T) and salinity (S) using the standard OCMIP carbonate chemistry routines¹. The routines used the carbonic acid dissociation constants of Mehrbach et al. (1973), as refit by Dickson and Millero (1987) and Dickson (1990). The pressure effect on the solubility was estimated from the equation of Mucci (1983), including the adjustments to the constants recommended by Millero (1995). Gas exchange is parameterized following Wanninkhof (1992), with the gas transfer velocity depending on the square of the wind speed. The reader interested in a more detailed description of the carbon biogeochemistry module is referred to Appendix A.

2.2 Forcing

Our analysis is primarily based on a transient simulation for the years 1995 to 2050 (Gruber et al., 2012), following the SRES A2 emissions scenario (Nakićenović and Swart, 2000) and on a time-slice simulation under preindustrial conditions (Hauri et al., 2009). For both simulations the physical part of the model remained the same. The model was forced at the surface with monthly climatologies of momentum fluxes computed from QuickSCAT-based Scatterometer Climatology of Ocean Winds (SCOW) (Risien and Chelton, 2008). The surface heat and freshwater fluxes were derived from the Comprehensive Ocean-Atmosphere Data Set (COADS) data products (da Silva et al., 1994) and applied with surface T and S restoring after Barnier et al. (1995) with a relaxation timescale of three months. To a limited extent, this approach allows to explicitly take into account riverine driven seasonal variability of S associated with the Columbia River, even though riverine input is not explicitly modeled. The initial and boundary conditions for T , S and nutrients were taken from the World Ocean Atlas

¹<http://www.ipsl.jussieu.fr/OCMIP/phase3/simulations/NOCES/HOWTO-NOCES-3.html>

**Variability and
long-term trends of
ocean acidification**

C. Hauri et al.

Title Page

Abstract

Introduction

Conclusions

References

Tables

Figures

◀

▶

◀

▶

Back

Close

Full Screen / Esc

Printer-friendly Version

Interactive Discussion



2005 (WOA05)². Monthly means of WOA05 were also used to prescribe T , S , and momentum fluxes along the three lateral open boundaries following a radiative scheme (Marchesiello et al., 2003). Initial and boundary conditions for DIC and Alk were taken from the GLobal Ocean Data Analysis Project (GLODAP, Key et al., 2004). A seasonal cycle was introduced in the DIC and Alk boundary conditions using a monthly climatology of $p\text{CO}_2$ (Takahashi et al., 2006) and a monthly climatology of surface Alk calculated using T and S following Lee et al. (2006). To estimate decreasing seasonal DIC and Alk variations with depth in subsurface waters, the seasonal amplitudes of DIC and Alk are scaled to the vertical profile of the seasonal amplitude of T . After a model spin up of 10 yr, the transient simulation was forced with increasing $p\text{CO}_2$ from 364 ppm in 1995 to 541 ppm in 2050, following the SRES A2 emissions scenario (Nakićenović and Swart, 2000), calculated from the NCAR CSM 1.4 carbon model output, which is a fully coupled Earth System Model (Frölicher et al., 2009). DIC concentrations at the lateral boundaries were prescribed to increase as well. We used the present-day DIC field from GLODAP as a basis and determined the annual increment of DIC from the NCAR CSM 1.4 carbon model simulation. DIC and atmospheric $p\text{CO}_2$ at the lateral boundaries were the only forcings that changed over the years. The climatologies for the lateral boundary conditions of Alk, T , S , nutrients and circulation remained unchanged from 2005 to 2050. For the pre-industrial time-slice simulation, the atmospheric $p\text{CO}_2$ was set to a preindustrial value (280 ppm), and the lateral DIC boundary conditions were taken from the preindustrial fields of GLODAP.

In order to analyze the sensitivity of our results towards the chosen SRES emissions scenario we compare the results of two additional transient simulations that follow both the “high- CO_2 ” SRES emissions scenario A2 described above, and the “low- CO_2 ” SRES emissions scenario B1 (Figs. A2 and A3). Due to computational constraints, these two additional simulations were conducted with a coarser-resolution setup of 15 km (Gruber et al., 2012). By 2050, atmospheric $p\text{CO}_2$ increased from 364 ppm

²http://www.nodc.noaa.gov/OC5/WOA05/pr_woa05.html

to 492 ppm in the B1 scenario, while in the A2 scenario atmospheric $p\text{CO}_2$ reached 541 ppm.

2.3 Study area

We focus our carbonate chemistry analysis on the nearshore area, within and just below the euphotic zone. We therefore chose the first 50 km in an east-west direction along the coast (Fig. 1, within light blue line), within which we analyze pH and Ω_{arag} at the surface and at 100 m depth. Since we are interested in the spatial variability of pH and Ω_{arag} , we chose not to average over the euphotic zone. We also divide the CCS into three subregions defined by Dorman and Winant (1995), based on distinct regional differences in the wind and temperature patterns. The region north of Cape Mendocino (40.5° N) is subsequently denoted as “northern” (blue), between Cape Mendocino and Point Conception (34.5° N) as “central” (orange) and south of Point Conception as “southern” (red) subregion (Fig. 1).

2.4 Temporal resolution of model output

The analysis of the trajectories of pH and Ω_{arag} from 2005 to 2050 is based on monthly modeled averages. Monthly time averaging reduces the aliasing of unresolved timescales that would result from monthly time-slices. Also, due to computational and storage constraints, two-day model output is produced for a limited time period only (2006–2010). To verify that a majority of the variability is retained by using monthly model output, we conducted spectral analysis of the two-day model output. We calculated the Welch power density spectrum (PDS) of the Fourier transform using a Hann window (Glover et al., 2011). The analysis was performed on detrended time-series data from each grid cell. The interval for the frequencies (f) captured with monthly output was set to $a = 0.2 \text{ yr}^{-1}$ and to $b = 6 \text{ yr}^{-1}$, according to thresholds given by the Nyquist-Shannon sampling theorem. For the frequencies captured with two-day output, the upper boundary was set to $c = 90 \text{ yr}^{-1}$. We quantified the amount of total variability

Variability and long-term trends of ocean acidification

C. Hauri et al.

Title Page

Abstract

Introduction

Conclusions

References

Tables

Figures



Back

Close

Full Screen / Esc

Printer-friendly Version

Interactive Discussion



across all frequencies from a to c and compared it to the amount of variability occurring in the frequencies from a to b . We define M as the percentage of the total variability of surface pH or Ω_{arag} that occurs at frequencies less than b as follows:

$$M = \frac{\int_a^b \text{PDS}(f) df}{\int_a^c \text{PDS}(f) df} \cdot 100 \quad (1)$$

M is plotted in Figs. 2a and 3a showing that in most areas (98.5 %) along the US West Coast the majority of variability of modeled pH and Ω_{arag} occurs at frequencies less than b and can be captured by monthly model output. However, as will be discussed in Sect. 4.1, high frequency variability can lead to very low pH and Ω_{arag} in some near shore surface areas. These few areas are constraint to about 1.5 % of the near-shore 50 km along the US West Coast. There, less than 50 % of the total variability of surface pH can be captured with monthly model output (Fig. 2a, blue). The time-series (Fig. 2b) and the power density spectrum of the Fourier transform (Fig. 2c) of two distinct example locations represent these two extreme cases: in location 1 (43°35' N, 124°45' W) the monthly averaged sampling frequency captures 89 %, whereas in location 2 (35°29' N, 121°34' W), only 49 % of the total variability of surface pH is captured with monthly modeled means. While in location 1 low-frequency modes below 2 months prevail (Fig. 2c, upper panel), high-frequency modes above 2 months are dominant in location 2 (Fig. 2c, lower panel). To fully capture the high frequency variability produced by the model for these areas, two-day model output would be required. At 100 m, the majority of variability of modeled Ω_{arag} occurs at frequencies less than b (Fig. 3a), with the low frequency variability of Ω_{arag} being the most dominant mode along the entire US West Coast (Fig. 3c).

To account for areas where the model variability of pH and Ω_{arag} are not fully captured with monthly output we introduce a correction factor (var_{cf}):

$$\text{var}_{\text{cf}} = \sqrt{\frac{\sigma_{\text{two-day}}^2}{\sigma_{\text{month}}^2}} \quad (2)$$

Variability and long-term trends of ocean acidification

C. Hauri et al.

Title Page

Abstract

Introduction

Conclusions

References

Tables

Figures



Back

Close

Full Screen / Esc

Printer-friendly Version

Interactive Discussion



where $\sigma_{\text{two-day}}^2$ is the temporal variance of the two-day output of model year 2010 and σ_{month}^2 is the temporal variance of the monthly averaged, two-day output data of the same year. The square root of the fraction is taken in order to apply it to the analysis of the transition decades in Sect. 4.4. The correction factor var_{cf} varies between 1.2 in the northern and southern CCS and 1.4 in the central CCS.

Additional high frequency variability in the field, due to synoptic wind driven upwelling, cannot be captured with either model output type due to our choice of monthly climatological wind forcing (see Sects. 3 and 5 for further discussion).

3 Model evaluation

The model's performance for simulating observed SST, surface chlorophyll and the mixed layer depth was already evaluated in Lachkar and Gruber (2011) and Gruber et al. (2006, 2011). The model represents the observed annual and seasonal patterns of surface temperature particularly well with a correlation of $r \sim 0.98$ and $r \sim 0.95$, respectively, and successfully captures the offshore extent of the cold upwelling region. The annual mean mixed-layer depth has a correlation of about 0.7 with observational data, but has a substantially higher standard deviation relative to the observations. The annual mean pattern of chlorophyll *a* compares well with the SeaWiFS data set ($r \sim 0.8$), however, with an underestimation of chlorophyll *a* in the near-shore 100 km and a poorer representation of its seasonal cycle ($r \sim 0.46$). The current paper will supplement this earlier evaluation by comparing the model to in situ data with an emphasis on vertical and cross-shore variability of the key carbonate chemistry properties in the upper ocean (also see Gruber et al., 2012).

First, we evaluate the modeled spatial variability of pH, Ω_{arag} , DIC, Alk, *T* and *S* by comparing it to ungridded data (Fig. 1, yellow dots, lines 4–11) from the North American Carbon Program (NACP) West Coast Cruise (Feely et al., 2008). The observational data was sampled between May and June of 2007.

BGD

9, 10371–10428, 2012

Variability and long-term trends of ocean acidification

C. Hauri et al.

Title Page

Abstract

Introduction

Conclusions

References

Tables

Figures

◀

▶

◀

▶

Back

Close

Full Screen / Esc

Printer-friendly Version

Interactive Discussion



To compare our model output to the observations, we averaged model output of May and June from 2006 to 2010 and linearly interpolated it to a vertical grid with 1 m resolution. A comparison of the modeled versus observed vertical distributions of the studied variables along a representative transect line (off Pt. St. George, California, Fig. 1, yellow arrow) indicates that the offshore pattern between 0–100 m is captured well (Fig. 4). However, the model underestimates the size of the vertical difference of DIC ($\sim 20 \mu\text{mol kg}^{-1}$) in waters deeper than ~ 125 m. In the nearshore region between 0–250 m depth, the model underestimates Alk by $10\text{--}35 \mu\text{mol kg}^{-1}$ and especially DIC by $40\text{--}150 \mu\text{mol kg}^{-1}$. The larger bias in DIC is the primary cause of the overestimation of the simulated pH (~ 0.2) and Ω_{arag} (~ 0.5), since their sensitivities towards changes in Alk and DIC are similar. As a result, our modeled aragonite saturation horizon is typically 60 m deeper than the observed one, and up to 150 m deeper during the strongest upwelling events. There is no obvious difference in model performance between subregions, i.e. pH and Ω_{arag} are modeled equally well for all three subregions with a correlation coefficient of about 0.89–0.90 between observed and modeled pH and 0.88–0.90 for Ω_{arag} (Fig. 5). The normalized standard deviation, correlation coefficient and bias between all observed and modeled properties can be found in Table A2.

The nearshore positive bias of pH and Ω_{arag} was introduced partially because transect line 5 was sampled during strong upwelling conditions (Feely et al., 2008). Such events are not simulated by our model since it is only forced with a monthly climatology of wind, but not with specific weather patterns and variability. The absence of such an intense upwelling event can be observed in all simulated variables shown in Fig. 4. The observed, strong outcrop nearshore indicates a vigorous upwelling, which is considerably underestimated by our model. This caveat was described by Gruber et al. (2006, 2012); Lachkar and Gruber (2011) and we focus on the implications of this discrepancy in the Discussion.

We evaluate the temporal variability of pH, Ω_{arag} , Alk, DIC, T and S using a bi-weekly climatology, sampled at the Santa Monica Bay Observatory Mooring at $33^{\circ}55.9' \text{N}$ and $118^{\circ}42.9' \text{W}$ from 2003 to 2008 (Leinweber and Gruber, 2012). Since interannual

BGD

9, 10371–10428, 2012

Variability and long-term trends of ocean acidification

C. Hauri et al.

Title Page

Abstract

Introduction

Conclusions

References

Tables

Figures

◀

▶

◀

▶

Back

Close

Full Screen / Esc

Printer-friendly Version

Interactive Discussion



anomalous weather patterns are not modeled, we produced a seasonal climatology of the observations from 2003 to 2008 and compared it to an averaged model output climatology of the same period.

As observed in the previous section the model underestimates pH and Ω_{arag} at depth (Fig. 6). The absolute levels of all properties in winter were well reproduced by the model at all depths. However, the observations show high temporal variability at the surface ($\text{pH} \pm 0.08$, 1 STD for the full observational record and $\Omega_{\text{arag}} \pm 0.4$) and at depth ($\text{pH} \pm 0.07$ and $\Omega_{\text{arag}} \pm 0.2$), which is underestimated by the model by a factor of about 7 for surface Ω_{arag} and by a factor of about 3.5 for surface pH and both variables at 100 m. The observed high spatial and temporal variability of pH and Ω_{arag} of the southern CCS is dominated by high frequency winds (Capet et al., 2004) that are not modeled with our set up. Moreover, in the model, the bottom topography is smoothed over the continental shelf to prevent numerical instabilities associated with complex bathymetry. Therefore, the variability resulting from the interaction of the flow field with the observed complex bathymetry, particularly in this region, is not fully represented.

A comparison with new pH and Ω_{arag} data derived from a surface mooring off Newport, OR ($44^{\circ}38'0''$ N $124^{\circ}18'13''$ W, Harris et al., 2012) from 2009 to 2011 demonstrates that the model does a good job in resolving the seasonal temporal variability in the northern CCS. There, the modeled temporal variability ($\text{pH} = 0.1$ and $\Omega_{\text{arag}} = 0.32$, 1 STD) agrees well with the observed temporal surface variability ($\text{pH} = 0.11$ and $\Omega_{\text{arag}} = 0.37$, 1 STD). Also, the model is in better agreement with the temporal variability of pH and Ω_{arag} in nearshore subsurface regions just north of Point Conception (Alin et al., 2012) than in the southern CCS. Alin et al. (2012) estimated pH and Ω_{arag} based on seasonal hydrographical data samples of CalCOFI line 76.7 from 2005 to 2010. Their estimated temporal variability of $\text{pH} = 0.09$ and $\Omega_{\text{arag}} = 0.32$ at 30 m depth are by a factor of 1.2 and 1.5, respectively, greater than the modeled temporal variability ($\text{pH} = 0.07$ and $\Omega_{\text{arag}} = 0.21$). These observation-model discrepancies increase with depth. At 100 m depth, the model underestimates the temporal variability of Ω_{arag} by a factor of 2 and by a factor of 5.5 for pH.

Variability and long-term trends of ocean acidification

C. Hauri et al.

Title Page

Abstract

Introduction

Conclusions

References

Tables

Figures

◀

▶

◀

▶

Back

Close

Full Screen / Esc

Printer-friendly Version

Interactive Discussion



In summary, there are two main model shortcomings that influence the results presented here (also see Discussion). pH and Ω_{arag} are overestimated at depth and in nearshore surface areas, resulting in a deeper aragonite saturation horizon than observed. Secondly, the modeled temporal variability of pH and Ω_{arag} is underestimated.

5 However, according to available observations, this bias is largest in the southern CCS and at depth and decreases towards the north.

4 Results

Here, we discuss the range and magnitude of changes in pH and Ω_{arag} and explore the drivers and mechanisms of the temporal and spatial variability in the nearshore environment of the CCS. We then present projections of the evolution of pH and Ω_{arag} trajectories until 2050 and determine the timing of when the subregions move out of their modeled preindustrial and projected present-day variability envelopes. Finally, we project when the absolute threshold of aragonite undersaturation is reached.

4.1 Spatial and temporal patterns of modeled pH and Ω_{arag}

15 Examples of the modeled monthly averages for surface pH of the model year 2011 ($p\text{CO}_2 \sim 395$ ppm) show that the waters within the first 50 km (here defined as nearshore) experience a wide range of surface pH from ~ 7.85 to 8.15 (Fig. 7a). The spatial variability of surface pH increases in April, when upwelling starts and is highest around July and August. The lowest surface pH (~ 7.85) is simulated nearshore between the Washington/Oregon border and Point Conception between June and September. The highest nearshore surface pH (~ 8.15) is reached between November and March in the northern subregion, while the central CCS only experiences high surface pH (~ 8.05) during 3 months (January–March). In the central CCS, surface pH decreases to ~ 7.95 around June and increases to around 8.05 in January. Further off
20 the coast, surface pH of the northern subregion remains at around 8.1, while in the
25

BGD

9, 10371–10428, 2012

Variability and long-term trends of ocean acidification

C. Hauri et al.

Title Page

Abstract

Introduction

Conclusions

References

Tables

Figures

◀

▶

◀

▶

Back

Close

Full Screen / Esc

Printer-friendly Version

Interactive Discussion



central and southern CCS it drops from ~ 8.15 to ~ 8.00 . At 100 m depth, low pH of about 7.75 extends to about 300 km offshore all year around, except along the Washington border, where pH remains close to about 8.1 between April and July, and drops to about 7.65 between August and October (not shown).

5 The seasonal evolution of surface Ω_{arag} behaves similarly to surface pH (not shown). The modeled monthly mean does not show undersaturation at the surface. However, model results from averaged two-day model output reveal that north of Cape Mendocino, surface pH can drop down to ~ 7.72 (Fig. 7c) and surface Ω_{arag} to 0.93, slightly below the values captured by the monthly mean outputs. In nearshore areas at 100 m
10 depth, aragonite undersaturation is also simulated in late fall, most likely due to remineralization of the sinking organic matter that was produced during the summer phytoplankton blooms (Fig. 7b).

4.2 Spatially averaged seasonal cycle of pH and Ω_{arag} for each subregion

15 The range of the mean seasonal cycle of pH and Ω_{arag} varies from region to region in the CCS (Fig. 8a and b) and is more pronounced at the surface than at 100 m. The northern subregion has the highest annual mean surface pH (~ 8.07) and the most distinct seasonal cycle (Fig. 8a), with a range of about ~ 0.14 pH units. In the central and southern CCS, the average surface pH is ~ 8.00 with a range of 0.09 and 0.04, respectively. While surface pH is lowest in August and September in the northern
20 subregion, the central subregion shows the lowest surface pH (~ 7.95) in June. Spatial variability of surface pH is highest in the central subregion ($\sim \pm 0.1$, 1 STD) around July, while it is small and constant in the southern subregion.

25 The annual mean surface Ω_{arag} is 2.02 in the northern and 1.88 in central CCS and is highest (~ 2.14) in the southern subregion (Fig. 8b). Surface Ω_{arag} decreases to ~ 1.85 in August and September in the northern subregion. The central subregion shows the lowest surface Ω_{arag} (~ 1.73) in June. In the southern CCS, surface Ω_{arag} increases slightly during the summer months. Surface Ω_{arag} of the northern and central CCS have

BGD

9, 10371–10428, 2012

Variability and long-term trends of ocean acidification

C. Hauri et al.

Title Page

Abstract

Introduction

Conclusions

References

Tables

Figures

◀

▶

◀

▶

Back

Close

Full Screen / Esc

Printer-friendly Version

Interactive Discussion



a spatial variability of $\sim \pm 0.4$ (1 STD) between April and October, which decreases to $\sim \pm 0.1$ (1 STD) in winter.

At 100 m depth, average pH remains around 7.8 and average Ω_{arag} around 1.1 in all three subregions. Spatial variability of both parameters and along the entire US West Coast is constant and small.

4.3 Mechanisms influencing the seasonal cycle in pH and Ω_{arag}

To understand the mechanisms causing changes in pH and Ω_{arag} across the seasonal cycles of the three subregions, we investigate the sensitivity of pH and Ω_{arag} to the seasonal variations in Alk, DIC, T and S . To do so, we estimate the contribution of changes in each property to the total change of pH and Ω_{arag} . The change in pH and Ω_{arag} can be "separated" using a Taylor expansion in first order of all constituting variables:

$$\Delta \text{pH} = \frac{\partial \text{pH}}{\partial \text{DIC}} \Delta_s \text{DIC} + \frac{\partial \text{pH}}{\partial \text{Alk}} \Delta_s \text{Alk} + \frac{\partial \text{pH}}{\partial T} \Delta T + \Delta \text{FS}_{\text{pH}} + \text{Res.} \quad (3)$$

where

$$\Delta \text{FS}_{\text{pH}} = \frac{\partial \text{pH}}{\partial S} \Delta S + \frac{\partial \text{pH}}{\partial \text{DIC}} \Delta \text{DIC}^s + \frac{\partial \text{pH}}{\partial \text{Alk}} \Delta \text{Alk}^s \quad (4)$$

and

$$\Delta \Omega = \frac{\partial \Omega}{\partial \text{DIC}} \Delta_s \text{DIC} + \frac{\partial \Omega}{\partial \text{Alk}} \Delta_s \text{Alk} + \frac{\partial \Omega}{\partial T} \Delta T + \Delta \text{FS}_{\Omega} + \text{Res.} \quad (5)$$

where

$$\Delta \text{FS}_{\Omega} = \frac{\partial \Omega}{\partial S} \Delta S + \frac{\partial \Omega}{\partial \text{DIC}} \Delta \text{DIC}^s + \frac{\partial \Omega}{\partial \text{Alk}} \Delta \text{Alk}^s \quad (6)$$

The partial derivatives quantify the differential changes in carbon chemistry due to small changes in DIC, Alk, T and S and are derived from model equations and annual means of a modeled climatology (2006–2010). $\Delta_s \text{DIC}$ and $\Delta_s \text{Alk}$ are the salinity

Variability and long-term trends of ocean acidification

C. Hauri et al.

Title Page

Abstract

Introduction

Conclusions

References

Tables

Figures

◀

▶

◀

▶

Back

Close

Full Screen / Esc

Printer-friendly Version

Interactive Discussion



Variability and long-term trends of ocean acidification

C. Hauri et al.

Title Page

Abstract

Introduction

Conclusions

References

Tables

Figures

◀

▶

◀

▶

Back

Close

Full Screen / Esc

Printer-friendly Version

Interactive Discussion



normalized deviations from the annual means of DIC and Alk; ΔDIC^S and ΔAlk^S are deviations from the annual means due to freshwater input, and $\Delta\text{FS}_{\text{pH}}$ and ΔFS_{Ω} are the total contributions of freshwater input to the change in pH and Ω_{arag} , respectively. The Taylor expansion is only strictly correct for small perturbations. Residuals (= Res.) thus capture the error when the left and right hand side of the equation are not equal.

pH and Ω_{arag} are driven by a combination of changes in DIC, Alk and T . These parameters are mainly altered by upwelling and eddies, which differ in magnitude and timing from region to region (Figs. 9 and 10). In addition, Alk changes due to the processes of nitrification, net primary production and CaCO_3 precipitation and dissolution (see Sect. 2.1 and Appendix A). DIC changes due to CaCO_3 calcification and dissolution, net primary production and heterotrophic respiration. Surface temperature is responsive to changes in the incoming solar radiation and heat exchange with the atmosphere. Figures 9 and 10 show the contributions of changes in DIC, Alk, S and T to changes (relative to the annual mean) in pH and Ω_{arag} , respectively. Each colored component represents the corresponding term in Eqs. (3) and (5). Components that plot in a positive direction have a positive effect on pH or Ω_{arag} . Therefore, the sum of all components lead to the total effect of pH and Ω_{arag} , resulting in either an addition or cancellation of the effect on pH or Ω_{arag} . pH is negatively correlated to changes in DIC, T and S , but has a positive correlation with changes in Alk. While the correlations for Ω_{arag} with Alk, DIC and S are the same as for pH, changes in Ω_{arag} are positively correlated to changes of T .

In the northern CCS, the effects of the changes in DIC and T on surface pH are cancelled by changes in Alk at the beginning of the upwelling season in spring and amplified in late summer and early fall (Fig. 9a). With a small delay, T amplifies the effect of changes in DIC on surface pH throughout the year. The upwelling of DIC-rich water decreases surface pH beginning in April. Due to a strong vertical Alk gradient, upwelled subsurface waters and primary production (Fig. A1a) increase Alk at the surface. The increase in Alk compensates for the upwelled DIC rich water and warming of the surface waters until the Alk concentration reaches its peak in August and dampens

the decrease of surface pH. As from August, net primary production (Fig. A1a) slows down and amplifies the negative effect of the upwelled, DIC enriched waters and of warm surface temperature, resulting in a minimum pH in August and September.

In the central CCS, upwelling starts in March, one month earlier than in the northern subregion (Fig. 9). The upwelled, DIC-enriched subsurface waters decrease surface pH to its minimum in June. In spring, DIC is the main driver of seasonal changes of pH. Decreased upwelling and increased primary production (Fig. A1a) decreases DIC as from August. Warming of the surface waters in late summer and fall cancels and delays the increasing effect of DIC on pH. In winter, T and Alk both amplify the effect of DIC, leading to a pH maximum in February.

In the southern CCS, changes in pH are mainly driven by the incoming solar radiation and heat exchange with the atmosphere (Fig. 9e), which decreases pH in summer, when sea surface temperature increases. The seasonal cycle of DIC is out of phase with the seasonal cycle of surface T and slightly counteracts the effect of T on pH. The warming of the surface waters lead to a late summer pH minimum.

At 100 m depth, the seasonal cycle of Alk in the northern CCS (Fig. 9b) is in concert with the seasonal cycle of DIC. The changes in Alk add to the effects of DIC on pH, while changes in temperature play a minor role. The absence of upwelling in the winter months leads to high pH levels in all subregions. Upwelling starts earlier in the southern (Fig. 9f) than northern CCS, shown by the earlier increase of DIC (decrease of pH) in the southern than in the northern subregion. In the central (Fig. 9d) and southern subregions, DIC is the main driver of pH, except during the upwelling season, when cold, upwelled waters counteract the effect of DIC on pH. The cold temperature of the upwelled waters dampen the early summer pH decrease in the central and southern CCS. Nitrification (Fig. A1b) sets in in March (southern CCS), in April (central CCS) or in June (northern CCS), decreases Alk and amplifies the decreasing effect of DIC on pH and counteracts the cold temperature effect.

The analysis of the contributions to the change in Ω_{arag} reveal that Alk has a much higher influence on Ω_{arag} in the northern subregion, than it does in the central or

BGD

9, 10371–10428, 2012

Variability and long-term trends of ocean acidification

C. Hauri et al.

Title Page

Abstract

Introduction

Conclusions

References

Tables

Figures

◀

▶

◀

▶

Back

Close

Full Screen / Esc

Printer-friendly Version

Interactive Discussion



southern CCS (Fig. 10). In the northern CCS, the upwelled Alk-enriched waters counteract the effect of upwelled DIC-rich waters, causing a peak of Ω_{arag} in April and May (Fig. 10a). The decrease of surface Ω_{arag} is thus delayed and changes in Ω_{arag} are suppressed. Because primary production slows down in August (Fig. A1a), Alk decreases and amplifies the effect of high DIC concentration on Ω_{arag} , causing its minimum in August. In the central and southern CCS, surface Ω_{arag} is mainly driven by the changes of DIC (Fig. 10c and e). Upwelling in the central subregion starts in April and increases surface DIC and thus decreases Ω_{arag} . The nutrient rich water enhances production, reaching its maximum in July (Fig. A1a). The decreasing primary production decreases Alk, which counteracts the positive effect on Ω_{arag} of a decreasing concentration of DIC due to decreased upwelling. Unlike for pH, surface water warming has a positive effect on Ω_{arag} in the southern CCS and amplifies the effects of the seasonal cycle of DIC.

At 100 m depth, Alk amplifies the effects of DIC on Ω_{arag} in all subregions (Fig. 10b, d, f). Respiration and nitrification (decrease of Alk) of sinking particles from the surface amplify the effects of the upwelled DIC-rich water, which leads to a minimum of Ω_{arag} at the end of the season (Fig. A1b).

4.4 Temporal and spatial variability vs. long-term trends

In this section, we determine the timing of transition periods under which the trajectories of pH and Ω_{arag} diverge from the ranges of variability that occurred during the preindustrial and the present-day time periods. To accomplish this, we define preindustrial (1750), present-day (2011), and future variability envelopes. These variability envelopes are computed by first computing the moving average (over a ten-year window) of the regional monthly time series model output. Secondly, we add and subtract the ten year moving standard deviation of the detrended regional monthly time series. As noted in Sect. 2, we correct the size of these modeled variability envelopes by a factor var_{cf} that accounts for our usage of monthly model output instead of the more variable two-day output. In a manner similar to Blackford and Gilbert (2007) and Cooley et al. (2012), we define the midpoint of a 10-yr transition period (transition decade) as the

BGD

9, 10371–10428, 2012

Variability and long-term trends of ocean acidification

C. Hauri et al.

Title Page

Abstract

Introduction

Conclusions

References

Tables

Figures

◀

▶

◀

▶

Back

Close

Full Screen / Esc

Printer-friendly Version

Interactive Discussion



point in time when the future envelope of pH or Ω_{arag} diverges from the preindustrial or present-day envelopes. While we report individual years for these transition decades below, it is important to recognize that they represent 10-yr windows within which these transitions are projected to take place.

5 Simulations following the SRES A2 emissions scenario show that increasing atmospheric CO_2 concentrations cause the pH and Ω_{arag} of the nearshore regions along the US West Coast to move out of their modeled preindustrial and projected present-day variability envelopes before 2050 (Figs. 11 and 12, orange and blue lines). By model year 2011, nearshore waters along the US West Coast have already moved out of the preindustrial envelope. In the northern CCS, pH has only recently departed from the preindustrial variability range due to its large temporal variability (Fig. 11a, upper panel). The strong projected decrease in pH forces the northern subregion to move out of its present-day variability envelope by 2045, despite the large variability. Surface pH in the central subregion is projected to depart from its present-day envelope by 2037 (Fig. 11a, center panel). Surface Ω_{arag} is projected to move out of its present-day envelope earlier than pH (Fig. 12a). Already by 2030, the northern CCS is projected to be exposed to lower levels of surface Ω_{arag} than experienced in 2011 (Fig. 12a, upper panel). Similarly, surface Ω_{arag} of the central subregion will depart from its present-day envelope by 2035 (Fig. 12a, center panel).

20 By 2023, surface pH and surface Ω_{arag} of the southern subregion are projected to decrease more than the range of their relatively small, modeled present-day variability (Figs. 11a and 12a, lower panels). However these results have to be taken with caution, since our model does not reproduce the large day to day variability observed in the southern CCS. We therefore expect that pH and Ω_{arag} in the southern subregion will remain within their natural variability envelopes longer than projected by the model (see Sect. 3 and Discussion).

25 At 100 m depth, pH and Ω_{arag} of the northern CCS are projected to depart from their modeled present-day variability envelopes by 2033, while in the central and southern this transition is projected to take place already by 2024 (Figs. 11b and 12b). In

BGD

9, 10371–10428, 2012

Variability and long-term trends of ocean acidification

C. Hauri et al.

Title Page

Abstract

Introduction

Conclusions

References

Tables

Figures

◀

▶

◀

▶

Back

Close

Full Screen / Esc

Printer-friendly Version

Interactive Discussion



addition, permanent undersaturation of Ω_{arag} at 100 m is projected before 2025 in the central and 2035 in the southern and northern CCS.

In a second simulation under which atmospheric CO_2 concentrations follow the “low- CO_2 ” (B1) emissions scenario, surface pH of the northern subregion will not move out of its present-day envelope before 2050 (see Fig. A2, upper panel). The projected lower atmospheric CO_2 concentrations, however, do not affect the timing of transition of Ω_{arag} in the north (Fig. A2, upper panel), and pH and Ω_{arag} in the central and southern CCS (Figs. A2a and A3a, centre and lower panels). This is because their variability range is low, leading to a departure from their variability envelopes before the atmospheric $p\text{CO}_2$ paths of the two emissions scenarios diverge around 2035 (Fig. S5 in Gruber et al., 2012).

The high spatial variability within each subregion (especially the northern subregion) leads to a large spatial difference in the arrival of the transition decades. Figures 13 and 14 illustrate the percentage of overlap between the variability range (mean \pm (1 STD \times var_{cf})) of a detrended 10 yr period from 2005 to 2015 of pH and Ω_{arag} , and the variability range for 10 yr periods of pH and Ω_{arag} for each following decade. The years 2020, 2030 and 2040 are chosen as midpoints for each 10 yr period. Nearshore areas, especially in the northern subregion, retain more than 50 % range overlap until 2030. These areas are exposed to the strongest upwelling and experience the largest range of pH and Ω_{arag} due to the upwelled cold, DIC and nutrient rich water. However, areas in the central CCS, south of Monterey Bay (36°48 N, 121°54 W), are projected to experience pH and Ω_{arag} values outside of the present-day range envelope by 2030. At 100 m depth, nearshore areas of the central and southern CCS are projected to be exposed to levels outside of the present-day range by 2020, while offshore areas retain some degree of overlap of range until 2030. In the northern subregion, the present-day range of pH and Ω_{arag} in nearshore regions still overlap by about 50 % until 2030.

BGD

9, 10371–10428, 2012

Variability and long-term trends of ocean acidification

C. Hauri et al.

Title Page

Abstract

Introduction

Conclusions

References

Tables

Figures

◀

▶

◀

▶

Back

Close

Full Screen / Esc

Printer-friendly Version

Interactive Discussion



4.5 Shoaling of the aragonite saturation horizon

In the central subregion, the modeled aragonite saturation horizon has already shoaled into the upper 100 m of the water column and is projected to reach a depth of 50 m by 2050 (Fig. 15a). The aragonite saturation horizon in the northern and southern CCS are projected to reach a depth of 100 m by 2025 and shoal to ~ 70 m depth by 2050. Figure 15b shows that after reaching the upper 100 m, the shoaling of the aragonite saturation horizon slows down substantially in all subregions. The saturation horizon is highly sensitive to changes in the concentration of CO_3^{2-} where the gradient of CO_3^{2-} concentration with respect to depth is small (Fig. 15). Conversely, when the CO_3^{2-} concentration gradient with respect to depth is strong, the saturation horizon is less sensitive to small changes of CO_3^{2-} concentration. As a result of these sensitivity differences, the aragonite saturation horizon shoals rapidly from 250 to 100 m because the CO_3^{2-} concentration gradient with respect to depth is small in this depth range. Once the saturation horizon enters the upper 100 m, it requires larger changes in CO_3^{2-} to lead to an equivalent shoaling of the aragonite saturation horizon. This explains why shoaling is initially rapid, and then slows down by about 2025, when the aragonite saturation horizon enters a depth range with larger gradients in CO_3^{2-} concentration.

5 Discussion

The comparison of our model results with available observations of nearshore carbon properties shows that the model is able to generally reproduce the large-scale spatial and seasonal patterns of contemporary pH and Ω_{arag} . However, the following caveats need to be borne in mind while discussing the annual cycle and future trajectories of pH and Ω_{arag} : (1) the model overestimates pH and Ω_{arag} off-shore and at a depth of 100–250 m, and in nearshore regions, (2) the model is forced with monthly climatologies of wind and cannot reproduce weather induced, high frequency events, (3) the riverine chemistry is not explicitly parameterized, (4) consequences of global change such as

BGD

9, 10371–10428, 2012

Variability and long-term trends of ocean acidification

C. Hauri et al.

Title Page

Abstract

Introduction

Conclusions

References

Tables

Figures

◀

▶

◀

▶

Back

Close

Full Screen / Esc

Printer-friendly Version

Interactive Discussion



changes in T , winds or precipitation are not taken into account, and (5) interannual processes such as El Niño/La Niña events are not resolved by the model.

Since the model overestimates pH and Ω_{arag} along the entire US West Coast, the annually averaged depth of the aragonite saturation horizon is expected to be about 60 m shallower in reality. Consequently, we expect that summertime undersaturation of surface waters in nearshore subregions of the northern and central CCS will happen more frequently and with a greater spatial extent than simulated by our model. Comparison to a Ω_{arag} timeseries derived from O_2 and S variability emphasizes this bias (Juraneck et al., 2009). Between May and November, their modeled aragonite saturation horizon remains within the upper 30 m of the water column. In contrast, our modeled saturation horizon shoals only occasionally into the upper 30 m and stays just above the Central Oregon shelf (~ 100 m) during the majority of the upwelling season. The depth bias between the observed and modeled aragonite saturation horizon is expected to decrease with time, because the shoaling of the aragonite saturation horizon is expected to slow down as it approaches shallower depths (see Sect. 4.5).

In our simulations day to day wind variability was not taken into account since the model was forced with a monthly climatology of momentum fluxes from QuickSCAT-based ocean winds. This does not present a large problem in the northern and central subregions where strong seasonal wind patterns prevail (Dorman and Winant, 1995). However, in the southern CCS it is synoptic variability that dominates the dynamics of the system (Leinweber et al., 2009; Dorman and Winant, 1995) and these features are not well captured by the monthly wind climatologies. As a result, the southern subregion is forced with unrealistically smooth wind patterns. Comparison with the Santa Monica Bay Observatory Mooring data underlines this shortcoming of our model for the southern CCS. The model underestimates pH variability (1 STD) by a factor of about ~ 3.5 . This implies that the projected transition decades would occur about 20 yr later than stated in our model results. Considering this caveat, the pH of the southern CCS would move out of its preindustrial envelope around 2020 and depart from the present-day levels shortly after 2050. The temporal variability of surface Ω_{arag} is

BGD

9, 10371–10428, 2012

Variability and long-term trends of ocean acidification

C. Hauri et al.

Title Page

Abstract

Introduction

Conclusions

References

Tables

Figures

◀

▶

◀

▶

Back

Close

Full Screen / Esc

Printer-friendly Version

Interactive Discussion



underestimated in the model by a factor of ~ 7 at the Santa Monica Bay Observatory Mooring, implying that the southern subregion won't move out of its preindustrial envelope before 2050. The comparison with observational data derived from the newly deployed mooring off Newport (Harris et al., 2012, see Sect. 3) and reconstructed pH and Ω_{arag} from T and O_2 time-series (Alin et al., 2012) indicate that our modeled size of the variability envelopes are in better agreement with the limited available data in the northern and central CCS than they are in the southern subregion. Taking advantage of the fast-growing US carbon mooring network in the future will help to further constrain the model bias and better predict the present-day variability envelope. Forcing the model with wind products at daily resolution could help to better simulate the observed high temporal variability in the winds and sporadic, strong upwelling events that cause extremely low levels of pH and Ω_{arag} .

Riverine input of nutrients, DIC and freshwater can increase the range of pH variability by up to about 1 unit (Hinga, 2002). Since the riverine chemistry is not explicitly modeled in this study, pH and Ω_{arag} may not be accurately represented in close proximity to the Columbia river mouth, especially during the rainy months (February–June). Other small rivers along the coast can influence DIC and Alk, however relative to the Columbia river their influence is small and often limited to infrequent storm events. The surface T and S restoring described in the methods section improves the mean state, but does not capture the natural variability.

Our study accounted for changes of pH and Ω_{arag} due to atmospheric $p\text{CO}_2$ increase, however, additional consequences of anthropogenic $p\text{CO}_2$ increase through its effects on the earth radiation balance, such as changes in upwelling intensity, strengthened stratification, warming of surface waters, deepening of the thermocline (King et al., 2011) and thus potential changes in the future seasonal cycle were not taken into account. Integrated effects of global change could possibly accelerate the progression of ocean acidification described here. For example, a timeseries (1982–2008) of upwelling favorable winds and sea surface T suggests that changes in T led to increased and protracted upwelling in parts of the central CCS (García-Reyes and

BGD

9, 10371–10428, 2012

Variability and long-term trends of ocean acidification

C. Hauri et al.

Title Page

Abstract

Introduction

Conclusions

References

Tables

Figures

◀

▶

◀

▶

Back

Close

Full Screen / Esc

Printer-friendly Version

Interactive Discussion



**Variability and
long-term trends of
ocean acidification**

C. Hauri et al.

Title Page

Abstract

Introduction

Conclusions

References

Tables

Figures

◀

▶

◀

▶

Back

Close

Full Screen / Esc

Printer-friendly Version

Interactive Discussion



Largier, 2010), which in turn would lead to lower surface pH and Ω_{arag} , further exacerbating the effects of increasing $p\text{CO}_2$ on the CCS. In addition to increased aragonite undersaturation, shoaling of low oxygen waters further minimizes habitats of sensitive organisms (Bograd et al., 2008; McClatchie et al., 2010). Oxygen declines in the CCS result from decreasing concentrations of oxygen in the Equatorial and Eastern Pacific (Stramma et al., 2008, 2010; Bograd et al., 2008). These oxygen declines are thought to be due to increased stratification resulting from global warming (Stramma et al., 2008). As a result of continued global warming and intensified upwelling, hypoxic areas are expected to further expand in the CCS in the future.

The dynamics of the CCS are strongly dependent on interannual climate modes such as El Niño/La Niña events, which are not resolved by our model. La Niña in 2010 uplifted the isopycnals in late summer and doubled the period of normal seasonal exposure to undersaturated conditions on the continental shelf (Nam et al., 2011). The season of occurrence of La Niña events is variable. It is therefore possible that La Niña amplifies the effect of natural seasonal upwelling, leading to more extreme hypoxic and aragonite undersaturated conditions. As a result, variability envelopes would be widened and transition decades would be delayed, while seasonal aragonite undersaturation would occur earlier.

We found that the CCS is approaching the combined thresholds of both chemical aragonite dissolution and the departure from its variability envelope with respect to pH and Ω_{arag} . The CCS thus joins the Arctic and the Southern Oceans as one of only a few known ocean regions presently approaching this dual threshold (Steinacher et al., 2009; McNeil and Matear, 2008). Therefore, organisms in these regions must adapt to conditions that are both inherently chemically challenging and significantly different from present conditions. In contrast, while locations such as ocean station ALOHA are projected to depart their variability envelope by 2020 (Cooley et al., 2012), the inherent chemical properties at these sites leave them far from aragonite undersaturation.

6 Conclusions

This study gives new insights into the spatial and temporal dynamics of pH and Ω_{arag} along the US West Coast. It further enables us to relate the present-day high spatial and temporal variability of pH and Ω_{arag} to their modeled preindustrial and projected future ranges of pH and Ω_{arag} . While a few nearshore areas of the central and northern subregions are presently exposed to temporary undersaturation, the model also highlights the fact that the nearshore ecosystems along the US West Coast are already exposed to pH and Ω_{arag} levels outside of the modeled preindustrial variability envelope. Additionally, as early as ~ 2040 , surface pH and Ω_{arag} of the nearshore US West Coast are projected to move out of the projected present-day variability envelope under increasing atmospheric CO_2 concentrations as projected from the IPCC SRES A2-Scenario.

The combination of naturally high DIC and the oceanic uptake of anthropogenic CO_2 drives the CCS towards undersaturation faster than other coastal areas (Blackford and Gilbert, 2007) and on a similar timescale as the Arctic and Southern Oceans. Despite the high annual variability, the absolute decrease of pH and Ω_{arag} is fast and significant enough to cause a departure from its present-day range by 2040. We conclude that these types of changes put the CCS particularly at risk to the effects of ocean acidification. Given the imminent departure from preindustrial envelopes, we speculate that these effects may already be well underway.

Marine ecosystems of the CCS are exposed to a variety of stress factors, many of which are projected to increase in the future. Along with the developing problem of ocean acidification, organisms will have to deal with warming of the waters, an expansion of hypoxic areas and changes of the vertical structure of the water column (Gruber, 2011; Doney et al., 2012). Furthermore, non climate change related impacts, such as pollution, eutrophication and overfishing further increase the vulnerability of the CCS ecosystems. Together, these stressors compound the challenges that many organisms

BGD

9, 10371–10428, 2012

Variability and long-term trends of ocean acidification

C. Hauri et al.

Title Page

Abstract

Introduction

Conclusions

References

Tables

Figures

◀

▶

◀

▶

Back

Close

Full Screen / Esc

Printer-friendly Version

Interactive Discussion



of the CCS will face in the coming decades and will necessitate rapid migration, acclimation or adaptation in order to cope with these changing environmental conditions.

Appendix A

Description of the carbon biogeochemistry module

- 5 The carbon biogeochemistry module adds the three new state variables DIC, Alk and CaCO_3 (D_{CaCO_3}) to the model. The conservation equation for any tracer concentration B is given by

$$\frac{\partial B}{\partial t} = \underbrace{\nabla \cdot \mathbf{K} \nabla B}_{\text{diffusion}} - \underbrace{\mathbf{u} \cdot \nabla_h B}_{\text{horiz. advection}} - \underbrace{\left(w + w^{\text{sink}} \right) \frac{\partial B}{\partial z}}_{\text{vert. advection \& sinking}} + \underbrace{J(B)}_{\text{source minus sink term}} \quad (\text{A1})$$

- 10 where \mathbf{K} is the eddy kinematic diffusivity tensor, ∇ is the 3-D gradient, ∇_h is the horizontal gradient, \mathbf{u} denotes the horizontal and w the vertical velocities of the fluid, and w^{sink} is the vertical sinking rate of all particulate pools, except zooplankton (see Table A1). $J(B)$ denotes the source minus sink term for each tracer, which are described in detail for DIC, Alk and D_{CaCO_3} in the following. The remaining source minus sink terms for the other model state variables are defined in Gruber et al. (2006).

BGD

9, 10371–10428, 2012

Variability and long-term trends of ocean acidification

C. Hauri et al.

Title Page

Abstract

Introduction

Conclusions

References

Tables

Figures

◀

▶

◀

▶

Back

Close

Full Screen / Esc

Printer-friendly Version

Interactive Discussion



The sources and sinks of DIC include net community production, gas exchange, and CaCO₃ formation and dissolution:

$$\begin{aligned}
 J(\text{DIC}) = & \underbrace{-\mu_P^{\max}(T, I) \cdot \gamma(\text{NO}_3^-, \text{NH}_4^+) \cdot P \cdot r_{\text{C:N}}}_{\text{net primary production}} \\
 & - \underbrace{k_{\text{CaCO}_3}^{\text{form}} \cdot \mu_P^{\max}(T, I) \cdot \gamma(\text{NO}_3^-, \text{NH}_4^+) \cdot P \cdot r_{\text{C:N}}}_{\text{CaCO}_3 \text{ formation}} \\
 & + \underbrace{k_{D_S}^{\text{remin}} D_S \cdot r_{\text{C:N}} + k_{D_L}^{\text{remin}} D_L \cdot r_{\text{C:N}}}_{\text{detritus remineralization}} + \underbrace{\eta_Z^{\text{metab}} Z \cdot r_{\text{C:N}}}_{\text{zooplankton respiration}} + \underbrace{k_{\text{CaCO}_3}^{\text{diss}} D_{\text{CaCO}_3}}_{\text{dissolution}} \quad (\text{A2}) \\
 & + \underbrace{k_{S_D}^{\text{remin}} S_D \cdot r_{\text{C:N}}}_{\text{sediment remineralization at } k=1} + \underbrace{k_{S_{\text{CaCO}_3}}^{\text{diss}} S_{\text{CaCO}_3} \cdot r_{\text{C:N}}}_{\text{sediment dissolution at } k=1} \\
 & + \underbrace{J^{\text{Gas}}}_{\text{gas exchange}}
 \end{aligned}$$

This equation follows the nomenclature used in Gruber et al. (2006). Symbols with parentheses, such as $\mu_P^{\max}(T, I)$ represent functions of the respective variables. J^{Gas} is the gas exchange flux described below (Eq. A3). The state variable associated with the function/parameter is denoted in the subscript, while the corresponding process is given in the superscript. The variables in the equation denote the following: I and T are light and temperature, respectively, P is the phytoplankton pool, Z is the zooplankton pool, D_S is the small detritus pool, D_L is the large detritus pool, D_{CaCO_3} is the CaCO₃ pool in the water column, S_D is the nitrogen and S_{CaCO_3} is the CaCO₃ pool in the sediment. All relevant parameters are described in Table A1. The carbon fluxes are tied to those of nitrogen with a fixed stoichiometric ratio $r_{\text{C:N}}$ of 106 : 16 (Redfield et al., 1963).

Net primary production is the sum of regenerated and new production and decreases the DIC pool. Depending on whether phytoplankton (P) take up NH_4^+ or NO_3^- , nitrogen

Variability and long-term trends of ocean acidification

C. Hauri et al.

Title Page

Abstract

Introduction

Conclusions

References

Tables

Figures

◀

▶

◀

▶

Back

Close

Full Screen / Esc

Printer-friendly Version

Interactive Discussion



Variability and long-term trends of ocean acidification

C. Hauri et al.

Title Page

Abstract

Introduction

Conclusions

References

Tables

Figures

◀

▶

◀

▶

Back

Close

Full Screen / Esc

Printer-friendly Version

Interactive Discussion



adds to either the regenerated or the new production flux, respectively. The modeled phytoplankton growth is limited by temperature (T), light (I) and the concentrations of NO_3^- and NH_4^+ . $\mu_P^{\max}(T, I)$ is the temperature-dependent, light limited growth rate of P under nutrient replete condition. $\gamma(\text{NO}_3^-, \text{NH}_4^+)$ is a non-dimensional nutrient limitation factor, with a stronger limitation for nitrate than ammonium, taking into account that P take up NH_4^+ preferentially over NO_3^- and that the presence of ammonium inhibits the uptake of nitrate by P . For a more detailed description of these limitation factors the reader is referred to Gruber et al. (2006).

Formation of D_{CaCO_3} also decreases the DIC pool and is parameterized as 7% of the net primary production, such that for each mole of organic carbon formed by net primary production, 0.07 mol of D_{CaCO_3} are formed. D_{CaCO_3} dissolves at a fixed dissolution rate of 0.0057 day^{-1} . This processes releases CO_3^{2-} , and thus adds to the DIC pool. The full source minus sink equation for D_{CaCO_3} is described below (Eq. A6).

Zooplankton (Z) are parameterized with one size class (mesozooplankton). The Z respiration from basal metabolism and remineralization processes increases the total DIC pool. Large detritus (D_L) is remineralized at a rate of 0.01 m day^{-1} and small detritus (D_S) at a rate of 0.03 m day^{-1} . The different state sinking speeds and remineralization rates of small and large detritus result in a large difference of the remineralization length scales of 30 m for D_S and 1000 m for D_L . As a consequence, D_L is rapidly transported to depths below the euphotic zone, while D_S is subjected to off-shore transport and not encountered in the ocean interior (Gruber et al., 2006).

The sediment is parameterized as a simple one layer model added to the bottom layer ($k = 1$) of the model. The sediment is represented by the state variables S_D (mmolN m^{-2}) and S_{CaCO_3} (mmolC m^{-2}). Once organic matter and CaCO_3 arrive at the sediment surface they are accumulated in the sediment layer. The accumulated organic matter and CaCO_3 are subjected to first-order decomposition reactions that release dissolved material into the deepest model layer $k = 1$ and thus back into the water column.

Gas exchange is parameterized following Wanninkhof (1992):

$$J^{\text{Gas}} = \text{CO}_2^{\text{sol}} \cdot k \cdot (\rho\text{CO}_2^{\text{air}} - \rho\text{CO}_2^{\text{ocean}}), \quad (\text{A3})$$

where

$$k = 0.31 \cdot u^2 (\text{Sc}/660)^{-1/2}. \quad (\text{A4})$$

⁵ CO_2^{sol} is the temperature and salinity dependent solubility of CO_2 , $\rho\text{CO}_2^{\text{air}}$ is the CO_2 partial pressure in the atmosphere and $\rho\text{CO}_2^{\text{ocean}}$ is the partial pressure of CO_2 in sea-water. Oceanic uptake of CO_2 increases DIC, while it does not influence Alk. Oceanic ρCO_2 is calculated from DIC, Alk, temperature and salinity using the standard OCMIP carbonate chemistry routines³. The routines used the carbonic acid dissociation constants of Mehrbach et al. (1973), as refit by Dickson and Millero (1987) and Dickson
¹⁰ (1990). The pressure effect on the solubility was estimated from the equation of Mucci (1983), including the adjustments to the constants recommended by Millero (1995). k is the gas transfer coefficient given by equation three in Wanninkhof (1992), which is dependent on the square of the instantaneous wind speed and the temperature dependent Schmidt number (Sc).
¹⁵

Alk increases due to the removal of NO_3^- (new production) and dissolution of CaCO_3 and decreases due to the formation of NO_3^- (nitrification) and formation of CaCO_3 :

³<http://www.ipsl.jussieu.fr/OCMIP/phase3/simulations/NOCES/HOWTO-NOCES-3.html>

BGD

9, 10371–10428, 2012

Variability and long-term trends of ocean acidification

C. Hauri et al.

Title Page

Abstract

Introduction

Conclusions

References

Tables

Figures

◀

▶

◀

▶

Back

Close

Full Screen / Esc

Printer-friendly Version

Interactive Discussion



$$\begin{aligned}
 J(\text{Alk}) = & \underbrace{+2 \cdot k_{\text{CaCO}_3}^{\text{diss}} D_{\text{CaCO}_3}}_{\text{dissolution}} + \underbrace{\mu_P^{\text{max}}(T, I) \cdot \gamma(\text{NO}_3^-) \cdot P \cdot r_{\text{C:N}}}_{\text{new production}} \\
 & + \underbrace{2 \cdot k_{\text{CaCO}_3}^{\text{diss}} S_{\text{CaCO}_3}}_{\text{sediment dissolution at } k=1} \\
 & - \underbrace{2 \cdot k_{\text{CaCO}_3}^{\text{form}} \cdot \mu_P^{\text{max}}(T, I) \cdot \gamma(\text{NO}_3^-, \text{NH}_4^+) \cdot P \cdot r_{\text{C:N}}}_{\text{CaCO}_3 \text{ formation}} - \underbrace{k^{\text{nitr}}(I) \cdot \text{NH}_4^+}_{\text{nitrification}}
 \end{aligned} \tag{A5}$$

5 Nitrification is light limited (I) and parameterized at a rate of 0.05 day^{-1} (see Gruber et al., 2006). CaCO_3 formation and dissolution processes change Alk twice as much as DIC. This can be explained from the definition of alkalinity (Dickson, 1981) where the addition (removal) of 1 mol of CO_3^{2-} results in a 2 mol change in Alk.

10 The concentration of CaCO_3 (mmolCm^{-3}) is dependent on net primary production and dissolution:

$$\begin{aligned}
 J(D_{\text{CaCO}_3}) = & \underbrace{k_{\text{CaCO}_3}^{\text{form}} \cdot \mu_P^{\text{max}}(T, I) \cdot \gamma(\text{NO}_3^-, \text{NH}_4^+) \cdot P \cdot r_{\text{C:N}}}_{\text{CaCO}_3 \text{ formation}} \\
 & - \underbrace{k_{\text{CaCO}_3}^{\text{diss}} D_{\text{CaCO}_3}}_{\text{dissolution}},
 \end{aligned} \tag{A6}$$

15 CaCO_3 increases by 0.07 mol ($k_{\text{CaCO}_3}^{\text{form}}$) for each mole of organic carbon produced by net primary production and it dissolves at a fixed rate of 0.0057 day^{-1} ($k_{\text{CaCO}_3}^{\text{diss}}$) in the water column and at 0.002 day^{-1} ($k_{\text{CaCO}_3}^{\text{diss}}$) in the sediment.

Acknowledgements. We are grateful to Damian Loher for support with the model simulations. We thank Thomas Frölicher, Fortunat Joos and Marco Steinacher who kindly provided us with results from their NCAR CSM 1.4-carbon model simulations. We would also like to thank Simone Alin and Katherine Harris for the observational data and Kay Steinkamp, Mark Payne and Diego Santaren for beneficial discussions and statistical support. C.H. was supported by the European Project of Ocean Acidification (EPOCA), which received funding from the European Community's Seventh Framework Programme (FP7/2007–2013) under grant agreement no. 211384. EPOCA is endorsed by the international programs Integrated Marine Biogeochemistry and Ecosystem Research (IMBER), Land-Ocean Interactions in the Coastal Zone (LOICZ), and Surface Ocean Lower Atmosphere Study (SOLAS). C. H., M. V., Z. L., A. M. P. M. and N. G. also acknowledge support by ETH Zurich. S. D. acknowledges support from NASA-NNX11AF55G.

References

- Alin, S. R., Feely, R. A., Dickson, A. G., Hernandez-Ayon, J. M., Juranek, L. W., Ohman, M. D., and Goericke, R.: Robust empirical relationships for estimating the carbonate system in the Southern California Current System and application to CalCOFI hydrographic cruise data (2005–2011), *J. Geophys. Res.*, 117, C05033, doi:10.1029/2011JC007511, 2012. 10375, 10384, 10395
- Barnier, B., Siefridt, L., and Marchesiello, P.: Thermal forcing for a global ocean circulation model using a three-year climatology of ECMWF analyses, *J. Marine Syst.*, 6, 363–380, doi:10.1016/0924-7963(94)00034-9, 1995. 10378
- Blackford, J. and Gilbert, F.: pH variability and CO₂ induced acidification in the North Sea, *J. Marine Syst.*, 64, 229–241, doi:10.1016/j.jmarsys.2006.03.016, 2007. 10390, 10397
- Bograd, S. J., Castro, C. G., Di Lorenzo, E., Palacios, D. M., Bailey, H., Gilly, W., and Chavez, F. P.: Oxygen declines and the shoaling of the hypoxic boundary in the California Current, *Geophys. Res. Lett.*, 35, L12607, doi:10.1029/2008GL034185, 2008. 10396
- Capet, X., Marchesiello, P., and McWilliams, J.: Upwelling response to coastal wind profiles, *Geophys. Res. Lett.*, 31, L13311, doi:10.1029/2004GL020123, 2004. 10384

Variability and long-term trends of ocean acidification

C. Hauri et al.

Title Page

Abstract

Introduction

Conclusions

References

Tables

Figures



Back

Close

Full Screen / Esc

Printer-friendly Version

Interactive Discussion



Variability and long-term trends of ocean acidification

C. Hauri et al.

[Title Page](#)
[Abstract](#)
[Introduction](#)
[Conclusions](#)
[References](#)
[Tables](#)
[Figures](#)
[Back](#)
[Close](#)
[Full Screen / Esc](#)
[Printer-friendly Version](#)
[Interactive Discussion](#)


- Cooley, S. R., Lucey, N., Kite-Powell, H., and Doney, S. C.: Nutrition and income from molluscs today imply vulnerability to ocean acidification tomorrow, *Fish Fish.*, 13, 182–215, doi:10.1111/j.1467-2979.2011.00424.x, 2012. 10376, 10390, 10396
- da Silva, A., Young, C., and Levitus, S.: Atlas of surface marine data 1994, Tech. Rep. Volume 1: Algorithms and procedures. Technical Report NOAA Atlas NESDIS 6, National Oceanic and Atmospheric Administration, Washington, DC, 1994. 10378
- Dickson, A.: An exact definition of total alkalinity and a procedure for the estimation of alkalinity and total inorganic carbon from titration data, *Deep-Sea Res.*, 28, 609–623, doi:10.1016/0198-0149(81)90121-7, 1981. 10402
- Dickson, A. G.: Thermodynamics of the dissociation of boric acid in synthetic seawater from 273.15 to 318.15 K, *Deep-Sea Res.*, 37, 755–766, doi:10.1016/0198-0149(90)90004-F, 1990. 10378, 10401
- Dickson, A. G. and Millero, F. J.: A comparison of the equilibrium constants for the dissociation of carbonic acid in seawater media, *Deep-Sea Res.*, 34, 1733–1743, doi:10.1016/0198-0149(87)90021-5, 1987. 10378, 10401
- Doney, S. C., Ruckelshaus, M., Duffy, J. E., Barry, J. P., Chan, F., English, C. A., Galindo, H. M., Grebmeier, J. M., Hollowed, A. B., Knowlton, N., Polovina, J., Rabalais, N. N., Sydeman, W. J., and Talley, L. D.: Climate change impacts on marine ecosystems, *Annu. Rev. Mar. Sci.*, 4, 11–37, doi:10.1146/annurev-marine-041911-111611, 2012. 10374, 10397
- Dorman, C. E. and Winant, C. D.: Buoy observations of the atmosphere along the west coast of the United States, 1981–1990, *J. Geophys. Res.*, 100, 16029–16044, doi:10.1029/95JC00964, 1995. 10375, 10380, 10394
- Feely, R. A., Sabine, C. L., Lee, K., Berelson, W., Kleypas, J., Fabry, V. J., and Millero, F. J.: Impact of anthropogenic CO₂ on the CaCO₃ system in the oceans, *Science*, 305, 362–366, doi:10.1126/science.1097329, 2004. 10374
- Feely, R. A., Sabine, C. L., Hernandez-Ayon, J. M., Ianson, D., and Hales, B.: Evidence for upwelling of corrosive “acidified” water onto the continental shelf, *Science*, 320, 1490–1492, doi:10.1126/science.1155676, 2008. 10374, 10375, 10382, 10383, 10410, 10414, 10415
- Friedrich, T., Timmermann, A., Abe-Ouchi, A., Bates, N. R., Chikamoto, M. O., Church, M. J., Dore, J. E., Gledhill, D. K., Gonzalez-Davila, M., Heinemann, M., Ilyina, T., Jungclaus, J. H., McLeod, E., Mouchet, A., and Santana-Casiano, J. M.: Detecting regional anthropogenic trends in ocean acidification against natural variability, *Nat. Clim. Change*, 2, 167–171, doi:10.1038/nclimate1372, 2012. 10376

Variability and long-term trends of ocean acidification

C. Hauri et al.

Title Page

Abstract

Introduction

Conclusions

References

Tables

Figures

◀

▶

◀

▶

Back

Close

Full Screen / Esc

Printer-friendly Version

Interactive Discussion



Frölicher, T., Joos, F., Plattner, G., Steinacher, M., and Doney, S.: Natural variability and anthropogenic trends in oceanic oxygen in a coupled carbon cycle–climate model ensemble, *Global Biogeochem. Cy.*, 23, GB1003, doi:10.1029/2008GB003316, 2009. 10379

García-Reyes, M. and Largier, J.: Observations of increased wind-driven coastal upwelling off central California, *J. Geophys. Res.*, 115, C04011, doi:10.1029/2009JC005576, 2010. 10395

Glover, D., Jenkins, W., and Doney, S.: *Modeling Methods for Marine Science*, Cambridge University Press, Cambridge, UK and New York, NY, USA, 996 pp., 2011. 10380

Gruber, N.: Warming up, turning sour, losing breath: ocean biogeochemistry under global change, *Philos. T. R. Soc. A*, 369, 1980–1996, doi:10.1098/rsta.2011.0003, 2011. 10397

Gruber, N., Frenzel, H., Doney, S. C., Marchesiello, P., McWilliams, J. C., Moisan, J. R., Oram, J. J., Plattner, G.-K., and Stolzenbach, K. D.: Eddy-resolving simulation of plankton ecosystem dynamics in the California Current System, *Deep-Sea Res.*, 53, 1483–1516, doi:10.1016/j.dsr.2006.06.005, 2006. 10376, 10377, 10382, 10383, 10398, 10399, 10400, 10402

Gruber, N., Lachkar, Z., Frenzel, H., Marchesiello, P., Munnich, M., McWilliams, J., Nagai, T., and Plattner, G.-K.: Eddy-induced reduction of biological production in Eastern Boundary Upwelling Systems, *Nat. Geosci.*, 4, 787–792, doi:10.1038/ngeo1273, 2011. 10377, 10382

Gruber, N., Hauri, C., Lachkar, Z., Loher, D., Frölicher, T. L., and Plattner, G.-K.: Rapid progression of ocean acidification in the California Current System, *Science*, 337, 220–223, doi:10.1126/science.1216773, 2012. 10374, 10375, 10377, 10378, 10379, 10382, 10383, 10392

Hales, B., Takahashi, T., and Bandstra, L.: Atmospheric CO₂ uptake by a coastal upwelling system, *Global Biogeochem. Cy.*, 19, GB1009, doi:10.1029/2004GB002295, 2005. 10374

Harris, K., DeGrandpre, M., and Hales, B.: Aragonite saturation states in a coastal upwelling zone, in preparation, 2012. 10384, 10395

Hauri, C., Gruber, N., Plattner, G.-K., Alin, S., Feely, R. A., Hales, B., and Wheeler, P. A.: Ocean acidification in the California Current System, *Oceanography*, 22, 58–69, doi:10.5670/oceanog.2009.97, 2009. 10375, 10378

Hinga, K. R.: Effects of pH on coastal marine phytoplankton, *Mar. Ecol.-Prog. Ser.*, 238, 281–300, doi:10.3354/meps238281, 2002. 10395

Juranek, L. W., Feely, R. A., Peterson, W. T., Alin, S. R., Hales, B., Lee, K., Sabine, C. L., and Peterson, J.: A novel method for determination of aragonite saturation state on the conti-

Variability and long-term trends of ocean acidification

C. Hauri et al.

[Title Page](#)
[Abstract](#)
[Introduction](#)
[Conclusions](#)
[References](#)
[Tables](#)
[Figures](#)
[Back](#)
[Close](#)
[Full Screen / Esc](#)
[Printer-friendly Version](#)
[Interactive Discussion](#)


mental shelf of Central Oregon using multi-parameter relationships with hydrographic data, *Geophys. Res. Lett.*, 36, L24601, doi:10.1029/2009GL040778, 2009. 10375, 10394

Key, R., Kozyr, A., Sabine, C., Lee, K., Wanninkhof, R., Bullister, J., Feely, R., Millero, F., Mordy, C., and Peng, T.-H.: A global ocean carbon climatology: results from Global Data Analysis Project (GLODAP), *Global Biogeochem. Cy.*, 18, GB4031, doi:10.1029/2004GB002247, 2004. 10379

King, J. R., Agostini, V. N., Harvey, C. J., McFarlane, G. A., Foreman, M. G. G., Overland, J. E., Di Lorenzo, E., Bond, N. A., and Aydin, K. Y.: Climate forcing and the California Current ecosystem, *ICES J. Mar. Sci.*, 68, 1199–1216, doi:10.1093/icesjms/fsr009, 2011. 10395

Kleypas, J., Feely, R., Fabry, V., Langdon, C., Sabine, C., and Robbin, L.: Impacts of Ocean Acidification on Coral Reefs and Other Marine Calcifiers: A Guide for Future Research, Report of a workshop held 18–20 April 2005, St. Petersburg, FL, sponsored by NSF, NOAA, and the US Geological Survey, 88 pp., 2006. 10374

Lachkar, Z. and Gruber, N.: What controls biological production in coastal upwelling systems? Insights from a comparative modeling study, *Biogeosciences*, 8, 2961–2976, doi:10.5194/bg-8-2961-2011, 2011. 10377, 10382, 10383

Lee, K., Tong, L., Millero, F., Sabine, C., Dickson, A., Goyet, C., Geun-Ha, P., Wanninkhof, R., Feely, R., and Key, R.: Global relationships of total alkalinity with salinity and temperature in surface waters of the world's oceans, *Geophys. Res. Lett.*, 33, L19605, doi:10.1029/2006GL027207, 2006. 10379

Leinweber, A. and Gruber, N.: High temporal variability of ocean acidification indicators in Santa Monica Bay, CA, in preparation, 2012. 10375, 10383

Leinweber, A., Gruber, N., Frenzel, H., Friedrichs, G. E., and Chavez, F.: Diurnal carbon cycling in the surface ocean and lower atmosphere of Santa Monica Bay, California, *J. Geophys. Res.*, 36, L08601, doi:10.1029/2008GL037018, 2009. 10394

Marchesiello, P., McWilliams, J., and Shchepetkin, A.: Equilibrium structure and dynamics of the California Current System, *J. Phys. Oceanogr.*, 33, 753–783, doi:10.1175/1520-0485(2003)33<753:ESADOT>2.0.CO;2, 2003. 10377, 10379

Martin, S. and Gattuso, J.-P.: Response of Mediterranean coralline algae to ocean acidification and elevated temperature, *Global Change Biol.*, 15, 2089–2100, doi:10.1111/j.1365-2486.2009.01874.x, 2009. 10374

Variability and long-term trends of ocean acidification

C. Hauri et al.

[Title Page](#)
[Abstract](#)
[Introduction](#)
[Conclusions](#)
[References](#)
[Tables](#)
[Figures](#)
[Back](#)
[Close](#)
[Full Screen / Esc](#)
[Printer-friendly Version](#)
[Interactive Discussion](#)


McClatchie, S., Goericke, R., Cosgrove, R., Auad, G., and Vetter, R.: Oxygen in the Southern California Bight: multidecadal trends and implications for demersal fisheries, *Geophys. Res. Lett.*, 37, L19602, doi:10.1029/2010GL044497, 2010. 10396

McNeil, B. I. and Matear, R. J.: Southern Ocean acidification: a tipping point at 450 ppm atmospheric CO₂, *P. Natl. Acad. Sci. USA*, 105, 18860–18864, doi:10.1073/pnas.0806318105, 2008. 10396

Mehrbach, C., Culbertson, C., and Hawley, J.: Measurement of the apparent dissociation constants of carbonic acid in seawater at atmospheric pressure, *Limnol. Oceanogr.*, 18, 897–907, 1973. 10378, 10401

Millero, F. J.: Thermodynamics of the carbon-dioxide system in the oceans, *Geochim. Cosmochim. Ac.*, 59, 661–677, doi:10.1016/0016-7037(94)00354-O, 1995. 10378, 10401

Mucci, A.: The solubility of calcite and aragonite in seawater at various salinities, temperatures, and one atmosphere total pressure, *Am. J. Sci.*, 283, 780–799, doi:10.2475/ajs.283.7.780, 1983. 10378, 10401

Nakićenović, N. and Swart, R.: Special Report on Emissions Scenarios: a Special Report of Working Group III of the Intergovernmental Panel on Climate Change, Cambridge Univ. Press, Cambridge, UK, pp. 20, 2000. 10375, 10378, 10379

Nam, S., Kim, H.-J., and Send, U.: Amplification of hypoxic and acidic events by La Niña conditions on the continental shelf off California, *Geophys. Res. Lett.*, 38, L22602, doi:10.1029/2011GL049549, 2011. 10396

Orr, J. C., Fabry, V. J., Aumont, O., Bopp, L., Doney, S. C., Feely, R. A., Gnanadesikan, A., Gruber, N., Ishida, A., Joos, F., Key, R. M., Lindsay, K., Maier-Reimer, E., Matear, R., Monfray, P., Mouchet, A., Najjar, R. G., Plattner, G.-K., Rodgers, K. B., Sabine, C. L., Sarmiento, J. L., Schlitzer, R., Slater, R. D., Totterdell, I. J., Weirig, M.-F., Yamanaka, Y., and Yool, A.: Anthropogenic ocean acidification over the twenty-first century and its impact on calcifying organisms, *Nature*, 437, 681–686, doi:10.1038/nature04095, 2005. 10374

Redfield, A. C., Ketchum, B. H., and Richards, F. A.: The influence of organisms on the composition of seawater, in: *The Sea*, vol. 2, edited by: Hill, M. N., Wiley Interscience, New York, pp. 26–77, 1963. 10377, 10399

Risien, C. and Chelton, D.: A global climatology of surface wind and wind stress fields from eight years of QuickSCAT scatterometer data, *J. Phys. Oceanogr.*, 38, 2379–2413, doi:10.1175/2008JPO3881.1, 2008. 10378

Variability and long-term trends of ocean acidification

C. Hauri et al.

Title Page

Abstract

Introduction

Conclusions

References

Tables

Figures

◀

▶

◀

▶

Back

Close

Full Screen / Esc

Printer-friendly Version

Interactive Discussion



- Sabine, C. L., Feely, R. A., Gruber, N., Key, R. M., Lee, K., Bullister, J. L., Wanninkhof, R., Wong, C. S., Wallace, D. W. R., Tilbrook, B., Millero, F. J., Peng, T.-H., Kozyr, A., Ono, T., and Rios, A. F.: The oceanic sink for anthropogenic CO₂, *Science*, 305, 367–371, doi:10.1126/science.1097403, 2004. 10374
- 5 Shchepetkin, A. and McWilliams, J.: The Regional Oceanic Modeling System (ROMS): a split-explicit, free-surface, topography-following-coordinate oceanic model, *Ocean Model.*, 9, 347–404, doi:10.1016/j.bbr.2011.03.031, 2005. 10377
- Steinacher, M., Joos, F., Frölicher, T. L., Plattner, G.-K., and Doney, S. C.: Imminent ocean acidification in the Arctic projected with the NCAR global coupled carbon cycle-climate model, *Biogeosciences*, 6, 515–533, doi:10.5194/bg-6-515-2009, 2009. 10396
- 10 Stramma, L., Johnson, G., Sprintall, J., and Mohrholz, V.: Expanding oxygen-minimum zones in the tropical oceans, *Science*, 320, 655–658, doi:10.1126/science.1153847, 2008. 10396
- Stramma, L., Schmidtko, S., Levin, L., and Johnson, G.: Ocean oxygen minima expansions and their biological impacts, *Deep-Sea Res.*, 57, 587–595, doi:10.1016/j.dsr.2010.01.005, 2010. 10396
- 15 Takahashi, T., Sutherland, S., Feely, R., and Wanninkhof, R.: Decadal change of the surface water pCO₂ in the North Pacific: a synthesis of 35 years of observations, *J. Geophys. Res.*, 111, C07S05, doi:10.1029/2005JC003074, 2006. 10379
- Taylor, K. E.: Summarizing multiple aspects of model performance in a single diagram, *J. Geophys. Res.*, 106, 1934–8592, doi:10.1029/2000JD900719, 2001. 10415
- 20 Wanninkhof, R.: Relationship between wind speed and gas exchange over the ocean, *J. Geophys. Res.*, 97, 7373–7382, doi:10.1029/92JC00188, 1992. 10378, 10401

Variability and long-term trends of ocean acidification

C. Hauri et al.

Title Page

Abstract

Introduction

Conclusions

References

Tables

Figures

◀

▶

◀

▶

Back

Close

Full Screen / Esc

Printer-friendly Version

Interactive Discussion



Table A1. Summary of the definitions, symbols, values and units of the parameters used in the carbon module of the ecological-biogeochemical model.

Parameter	Symbol	Value	Units
Fixed carbon to nitrogen ratio	$r_{C:N}$	6.25	–
Remineralization and respiration parameters			
Remineralization rate of D_S	$k_{D_S}^{remin}$	0.03	day^{-1}
Remineralization rate of D_L	$k_{D_L}^{remin}$	0.01	day^{-1}
Zooplankton basal metabolism rate	η_Z^{metab}	0.1	day^{-1}
CaCO ₃ formation and dissolution parameters			
CaCO ₃ fraction of net primary production	$k_{CaCO_3}^{form}$	0.07	–
CaCO ₃ dissolution rate	$k_{CaCO_3}^{diss}$	0.0057	day^{-1}
Sediment parameters			
Sediment remineralization	$k_{S_D}^{remin}$	0.003	day^{-1}
Sediment dissolution	$k_{S_{CaCO_3}}^{diss}$	0.002	day^{-1}
Sinking parameters			
Sinking velocity of P	W_P^{sink}	0.5	m day^{-1}
Sinking velocity of D_S	$W_{D_S}^{sink}$	1.0	m day^{-1}
Sinking velocity of D_L	$W_{D_L}^{sink}$	10.0	m day^{-1}
Sinking velocity of D_{CaCO_3}	$W_{D_{CaCO_3}}^{sink}$	20.0	m day^{-1}

Variability and long-term trends of ocean acidification

C. Hauri et al.

Table A2. Spatial model evaluation statistics. Shown are the normalized model standard deviation (norm. STD.), the correlation coefficient and bias of observed and modeled pH, Ω_{arag} , Alkalinity, DIC, Temperature and Salinity. A five year average of modeled parameters over May and June (2006–2010) are compared to observations sampled between May and June 2007 (Feely et al., 2008), for all sampled locations (CCS), the subregions north, central, southern, for 0–100 m, 100–250 m and 500–5000 m. The modeled standard deviations were normalized relative to the observed standard deviations from Feely et al. (2008). Specified units correspond only to the absolute bias.

Property	Location	norm. STD	Correlation Coefficient	absolute Bias
pH	CCS	0.74	0.89	−0.06
	northern	0.73	0.91	−0.07
	central	0.76	0.89	−0.05
	southern	0.71	0.89	−0.07
	0–100 m	0.58	0.74	−0.04
	100–250 m	0.33	0.43	−0.10
	250–4500 m	0.91	0.68	−0.09
Ω Aragonite	CCS	0.83	0.89	−0.11
	northern	0.79	0.91	−0.11
	central	0.87	0.89	−0.09
	southern	0.82	0.88	−0.12
	0–100 m	0.64	0.74	−0.08
	100–250 m	0.52	0.58	−0.15
	250–4500 m	1.37	0.83	−0.11
Alkalinity ($\mu\text{mol kg}^{-1}$)	CCS	0.88	0.92	−6
	northern	0.77	0.93	−20
	central	0.95	0.92	−4
	southern	1.04	0.94	−1
	0–100 m	0.40	0.79	−6
	100–250 m	0.63	0.68	−6
	250–4500 m	0.99	0.99	−8
DIC ($\mu\text{mol kg}^{-1}$)	CCS	0.87	0.92	14
	northern	0.79	0.93	3
	central	0.91	0.92	12
	southern	0.91	0.93	21
	0–100 m	0.56	0.77	10
	100–250 m	0.57	0.69	22
	250–4500 m	1.21	0.98	13
Temperature ($^{\circ}\text{C}$)	CCS	1.15	0.95	−0.31
	northern	1.05	0.95	−0.03
	central	1.15	0.93	−0.31
	southern	1.18	0.95	−0.47
	0–100 m	0.97	0.85	−0.90
	100–250 m	1.13	0.88	0.40
	250–4500 m	0.87	0.99	0.44
Salinity (PSU)	CCS	0.78	0.86	0.18
	northern	0.69	0.88	0.004
	central	0.91	0.83	0.20
	southern	1.14	0.86	0.26
	0–100 m	0.50	0.87	0.21
	100–250 m	0.71	0.88	0.22
	250–4500 m	0.90	1.08	0.04

Title Page

Abstract

Introduction

Conclusions

References

Tables

Figures

◀

▶

◀

▶

Back

Close

Full Screen / Esc

Printer-friendly Version

Interactive Discussion



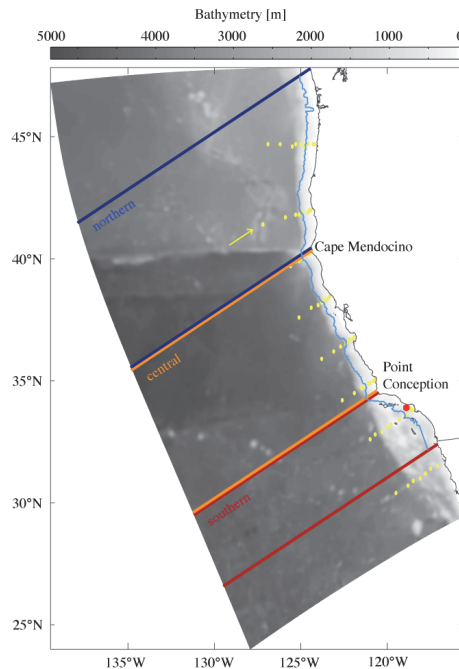


Fig. 1. US West Coast configuration of ROMS. The northern subregion is defined by the dark blue box and represents the area between the northern boundary of 47.5° N and a southern boundary at Cape Mendocino (40.5° N). Between Cape Mendocino and Point Conception (34.5° N) the central subregion is defined by the orange box. The southern subregion extends southwards from Point Conception to 32.4° N. The light blue line defines the study area of 50 km along the coast. Because of the perpendicular orientation of the regional boundaries the offshore part of each region's lower boundary lays south of the above mentioned latitudes. The yellow dots indicate the locations used in the model-observational data spatial comparison (see Sect. 3). The arrow is pointed at the transect used for visual comparison. The Santa Monica Bay Observatory Mooring ($33^{\circ}55.9'$ N and $118^{\circ}42.9'$ W) is shown as a red dot.

Variability and long-term trends of ocean acidification

C. Hauri et al.

Title Page

Abstract Introduction

Conclusions References

Tables Figures

◀ ▶

◀ ▶

Back Close

Full Screen / Esc

Printer-friendly Version

Interactive Discussion



Variability and long-term trends of ocean acidification

C. Hauri et al.

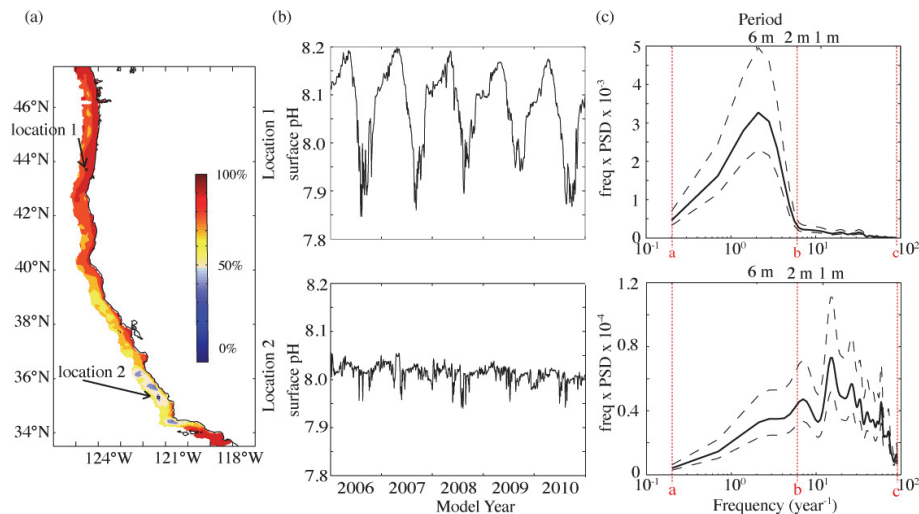


Fig. 2. Analysis of variability of surface pH. **(a)** indicates the percentage of the total variability of surface pH that occurs at frequencies less than $b = 6 \text{ yr}^{-1}$. The arrows point out the locations of the two example sites described in panels **(b)** and **(c)**. **(b)** Time-series of surface pH over 5 yr for two distinct example locations and **(c)** a variance conserving plot of the frequency \times power density spectrum (PDS) vs. the frequency of the Fourier transformed time-series. The black solid line represents the PDS and the black dashed lines envelope the $\pm 95\%$ confidence interval. The red dashed lines show the boundaries a , b and c of the integrals applied in Eq. (1).

Title Page

Abstract

Introduction

Conclusions

References

Tables

Figures

◀

▶

◀

▶

Back

Close

Full Screen / Esc

Printer-friendly Version

Interactive Discussion



Variability and long-term trends of ocean acidification

C. Hauri et al.

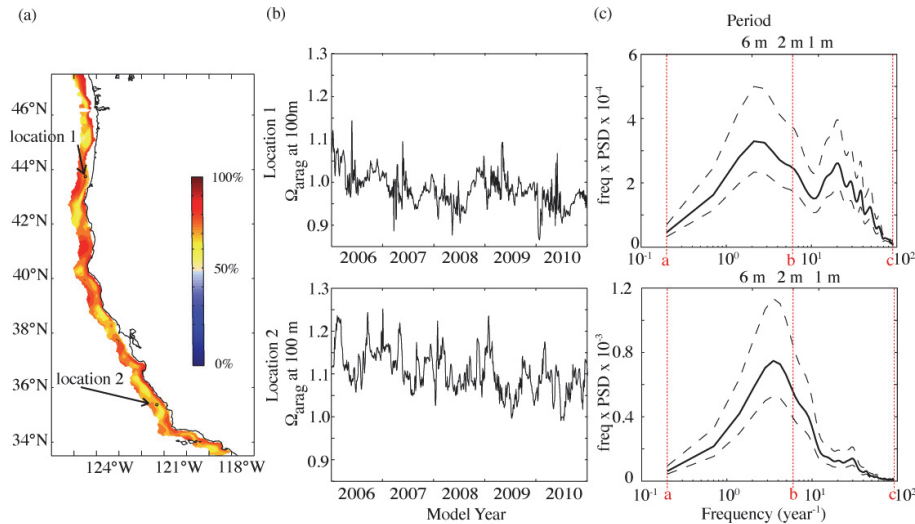


Fig. 3. Analysis of variability of Ω_{arag} at 100 m. **(a)** indicates the percentage of the total variability of Ω_{arag} at 100 m that occurs at frequencies less than $b = 6 \text{ yr}^{-1}$. The arrows point out the locations of the two example sites described in panels **(b)** and **(c)**. **(b)** Time-series of Ω_{arag} at 100 m over 5 yr for two distinct example locations and **(c)** a variance conserving plot of the frequency \times power density spectrum (PDS) vs the frequency of the Fourier transformed time-series. The black solid line represents the PDS and the black dashed lines envelope the $\pm 95\%$ confidence interval. The red dashed lines show the boundaries a , b and c of the integrals applied in Eq. (1).

Title Page

Abstract Introduction

Conclusions References

Tables Figures

◀ ▶

◀ ▶

Back Close

Full Screen / Esc

Printer-friendly Version

Interactive Discussion



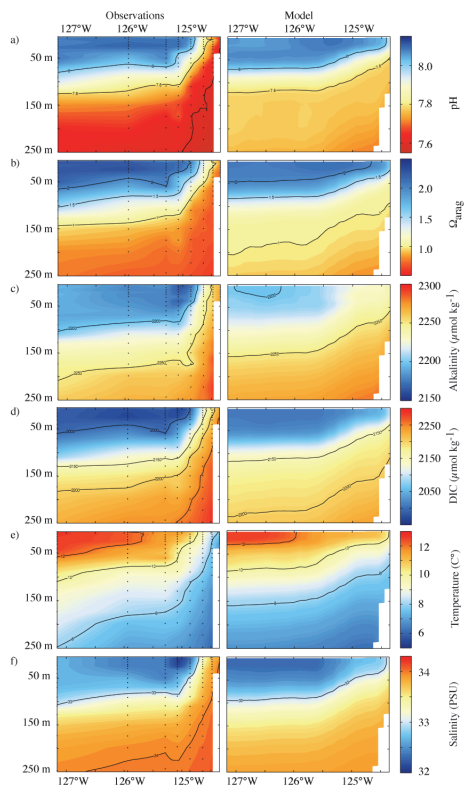


Fig. 4. Vertical sections of (a) pH, (b) Ω_{arag} , (c) alkalinity, (d) DIC, (e) temperature and (f) salinity of observations (left, Feely et al., 2008) and the corresponding model output (right), off Pt. St. George, California. A five year average of model parameters over May and June (2006–2010) is compared to observations sampled between May and June 2007. The black dots represent sample locations.

Variability and long-term trends of ocean acidification

C. Hauri et al.

Title Page

Abstract Introduction

Conclusions References

Tables Figures

◀ ▶

◀ ▶

Back Close

Full Screen / Esc

Printer-friendly Version

Interactive Discussion



Variability and long-term trends of ocean acidification

C. Hauri et al.

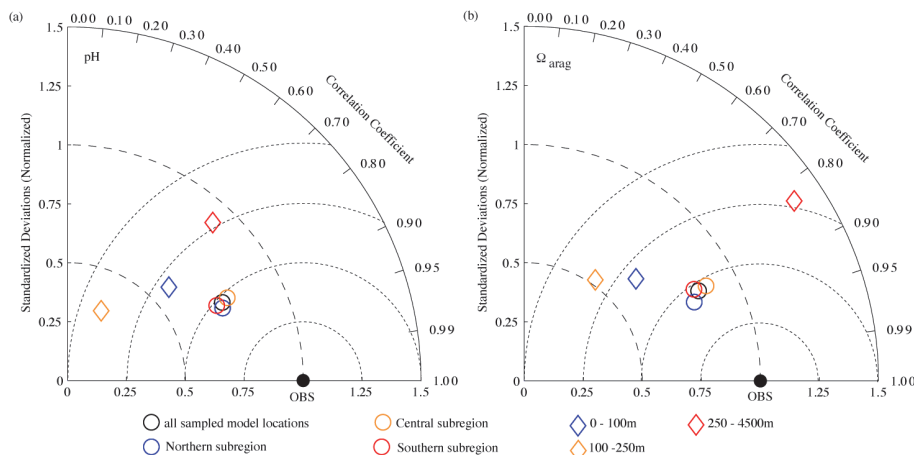


Fig. 5. Taylor diagram (Taylor, 2001) of model simulated (a) pH and (b) Ω_{arag} compared to observations (Feely et al., 2008). A five year average of parameters over May and June (2006–2010) are compared to observations sampled between May and June 2007, for all sampled locations (black), the northern (blue circle), central (orange circle), and southern subregions (red circle), and for 0–100 m (blue diamond), 100–250 m (orange diamond) and 500–5000 m (red diamond). The distance from the origin is the normalized standard deviation of the modeled parameters. The azimuth angle represents the correlation between the observations and the modeled parameters. The distance between the model point and the observation point (filled ellipse on the abscissa) indicates the normalized root mean square (RMS) misfit between model and observational estimates.

Title Page

Abstract

Introduction

Conclusions

References

Tables

Figures

◀

▶

◀

▶

Back

Close

Full Screen / Esc

Printer-friendly Version

Interactive Discussion



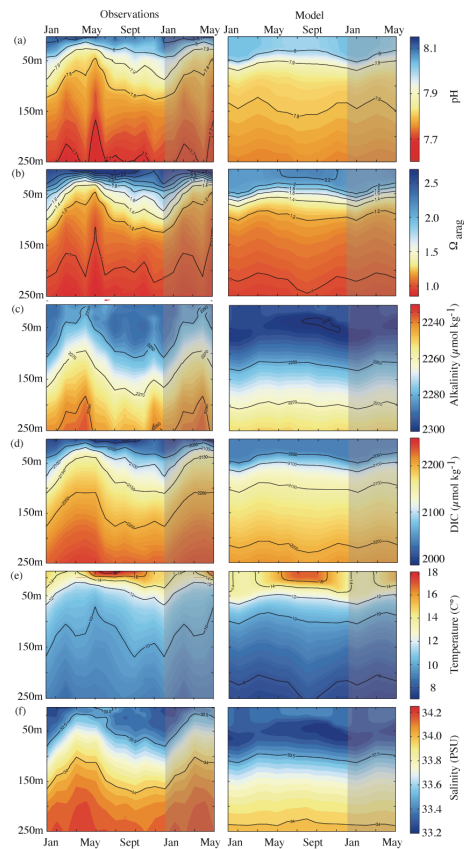


Fig. 6. Comparison of bi-weekly observed (2003–2008; Santa Monica Bay Observatory Mooring) and model simulated climatologies of **(a)** Ω_{arag} , **(b)** pH, **(c)** alkalinity, **(d)** DIC, **(e)** temperature and **(f)** salinity at 0–250 m between 2005 and 2010. The shaded area depicts the first six months of the following annual cycle.

Variability and long-term trends of ocean acidification

C. Hauri et al.

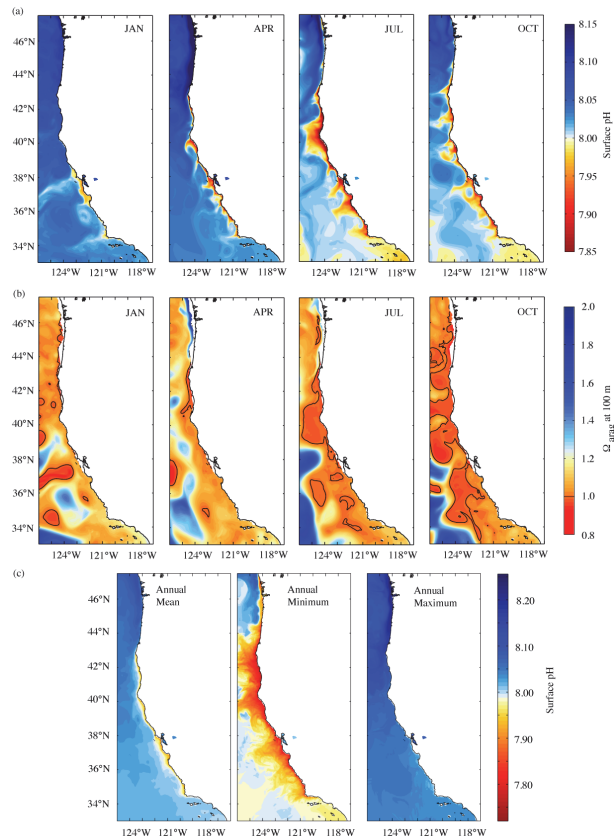


Fig. 7. Simulated monthly averages of (a) surface pH and (b) Ω_{arag} at 100 m. Shown are January, April, July and October of model year 2011 (~ 395 ppm atmospheric $p\text{CO}_2$). (c) Mean, minimum and maximum values of surface pH from two-day model output.

Variability and long-term trends of ocean acidification

C. Hauri et al.

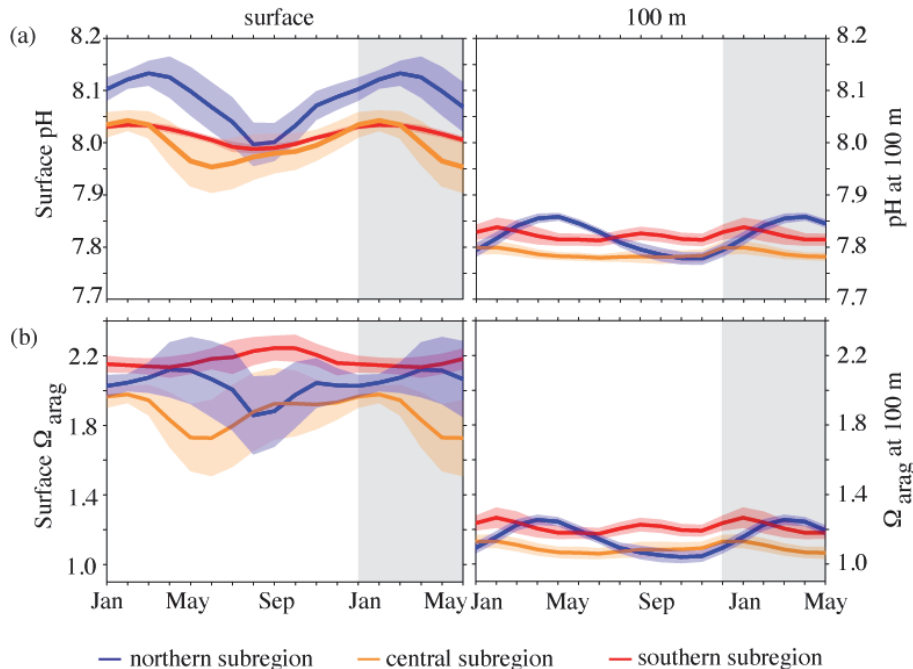


Fig. 8. Seasonal cycle of **(a)** pH and **(b)** Ω_{arag} in the nearshore 50 km. The lines represent the mean and the shaded area the spatial variability (± 1 STD) for each month, for the northern (blue), central (orange) and southern (red) subregions, at the surface (left) and at 100 m (right). The shaded area depicts the first six months of the following annual cycle.

Title Page

Abstract

Introduction

Conclusions

References

Tables

Figures

◀

▶

◀

▶

Back

Close

Full Screen / Esc

Printer-friendly Version

Interactive Discussion



Variability and long-term trends of ocean acidification

C. Hauri et al.

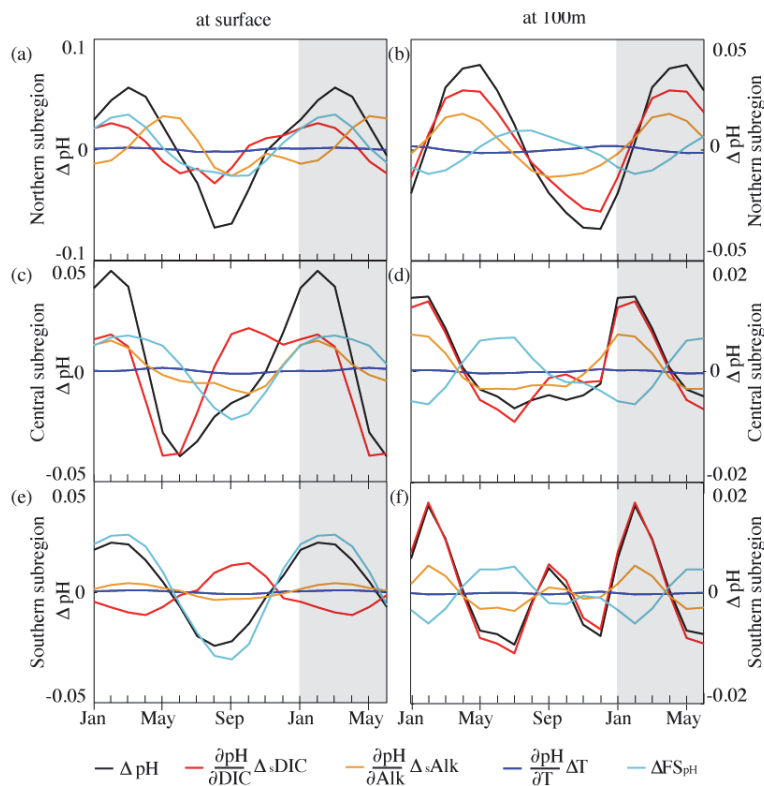


Fig. 9. Contributions of changes in DIC (red), alkalinity (orange), salinity (blue, freshwater flux, FS) and temperature (light blue) to changes (relative to the annual mean) in pH at the surface and at 100 m depth for the northern (top panels, **a** and **b**), central (center panels, **c** and **d**) and southern (bottom panels, **e** and **f**) subregions. Note different y-axis scales. The shaded area depicts the first six months of the following annual cycle.

Title Page

Abstract

Introduction

Conclusions

References

Tables

Figures

◀

▶

◀

▶

Back

Close

Full Screen / Esc

Printer-friendly Version

Interactive Discussion

Variability and long-term trends of ocean acidification

C. Hauri et al.

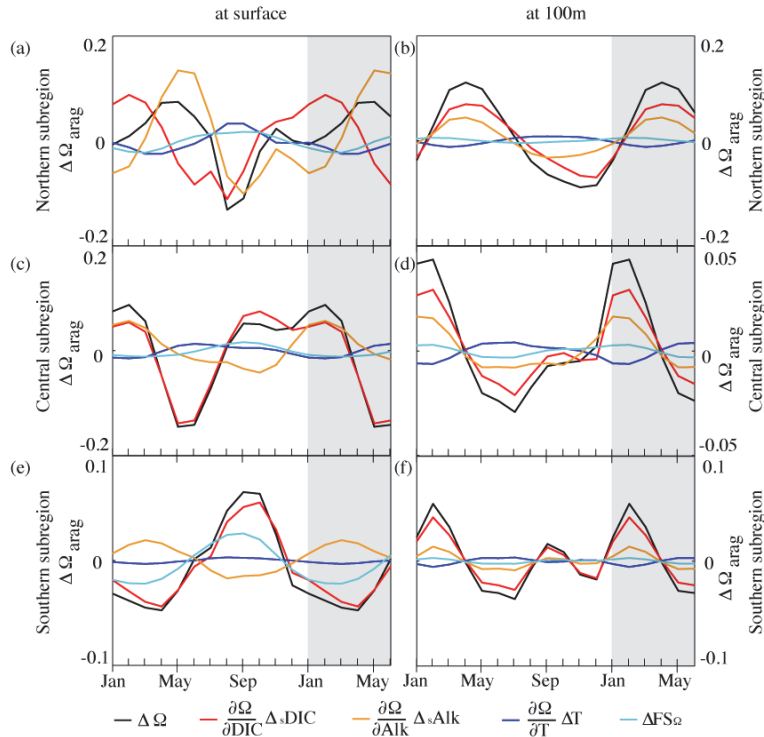


Fig. 10. Contributions of changes in DIC (red), alkalinity (orange), salinity (blue, freshwater flux, FS) and temperature (light blue) to changes (relative to the annual mean) in Ω_{arag} at the surface and at 100 m depth for the northern (top panels, **a** and **b**), central (center panels, **c** and **d**) and southern (bottom panels, **e** and **f**) subregions. Note different y-axis scales. The shaded area depicts the first six months of the following annual cycle.

Title Page

Abstract

Introduction

Conclusions

References

Tables

Figures

◀

▶

◀

▶

Back

Close

Full Screen / Esc

Printer-friendly Version

Interactive Discussion



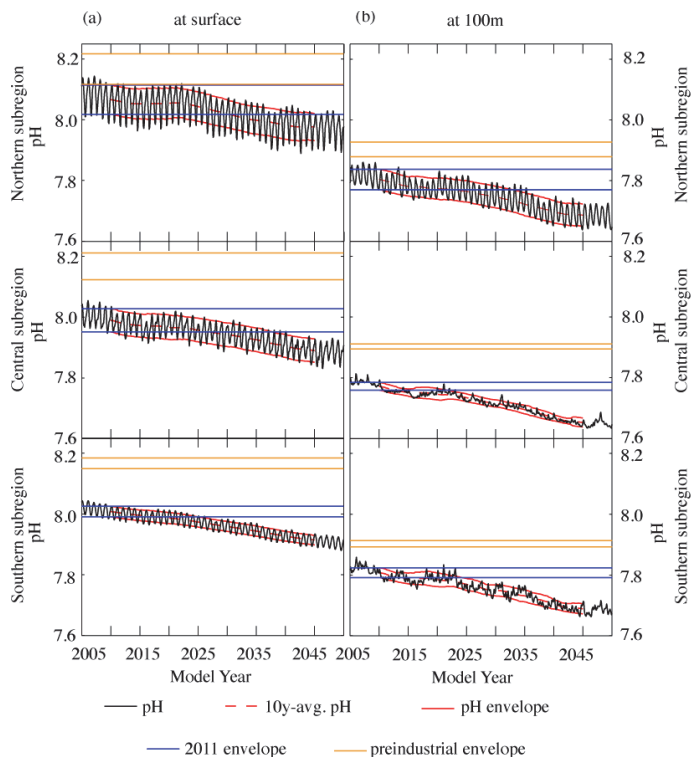


Fig. 11. Simulated timeseries of monthly mean pH (black) at **(a)** the surface and **(b)** 100 m depth, for the northern (top panel), central (center panel) and southern (bottom panel) subregions, with the 10-yr running average (red dashed line) for all grid cells of each subregion. The area between the solid lines defines the range of annual variability or envelope ($\text{mean} \pm (1 \text{ STD} \times \text{var}_{\text{cf}})$) of pH for the preindustrial (orange, ~ 270 ppm atmospheric $p\text{CO}_2$), 2011 (black, ~ 395 ppm atmospheric $p\text{CO}_2$) and transient (red) simulations. The envelopes are adjusted with the correction factor var_{cf} (Sect. 2.4).

Variability and long-term trends of ocean acidification

C. Hauri et al.

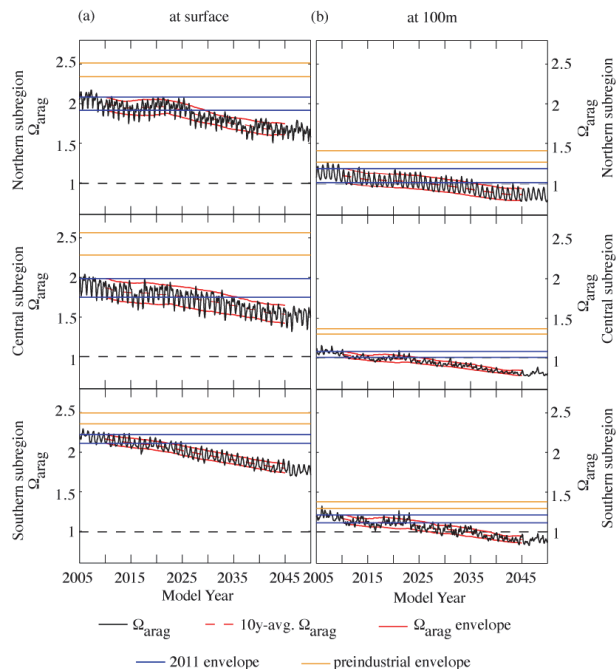


Fig. 12. Simulated timeseries of monthly mean Ω_{arag} (black) at **(a)** the surface and **(b)** 100 m depth, for the northern (top panel), central (center panel) and southern (bottom panel) subregions, with the 10-yr running average (red dashed line) for all grid cells of each subregion. The area between the solid lines defines the range of annual variability or envelope (mean \pm (1 STD \times var_{cf})) of Ω_{arag} for the preindustrial (orange, \sim 270 ppm atmospheric $p\text{CO}_2$), 2011 (black, \sim 395 ppm atmospheric $p\text{CO}_2$) and transient (red) simulations. The saturation horizon ($\Omega_{\text{arag}} = 1$) is indicated by the black dashed line. The envelopes are adjusted with the correction factor var_{cf} (Sect. 2.4).

[Title Page](#)
[Abstract](#)
[Introduction](#)
[Conclusions](#)
[References](#)
[Tables](#)
[Figures](#)
[Back](#)
[Close](#)
[Full Screen / Esc](#)
[Printer-friendly Version](#)
[Interactive Discussion](#)

Variability and long-term trends of ocean acidification

C. Hauri et al.

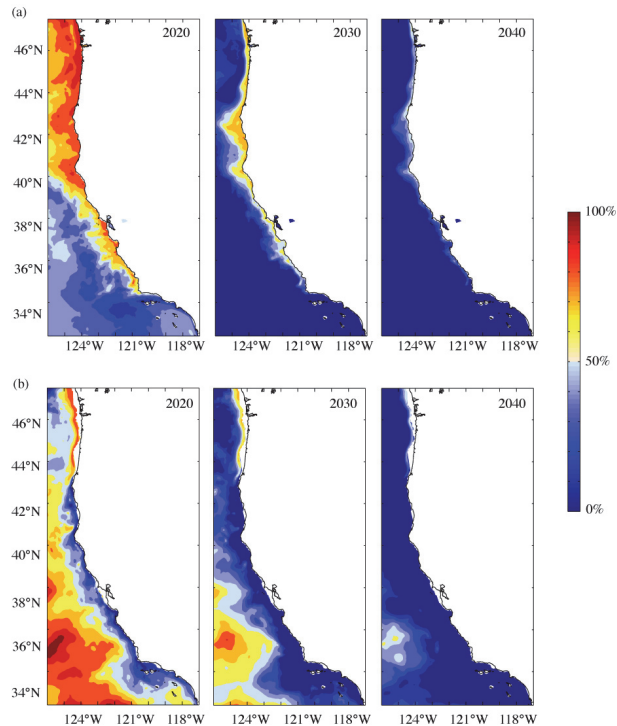


Fig. 13. The proportion of overlap in annual pH range (mean \pm (1 STD \times var_{cf})) of a ten year average at present for (a) the surface and (b) at 100 m depth, compared to ten year averages of every following decade until 2040. The years shown are the midpoints of the ten year average. The envelopes are adjusted with the correction factor var_{cf} (Sect. 2.4).

Title Page

Abstract

Introduction

Conclusions

References

Tables

Figures

◀

▶

◀

▶

Back

Close

Full Screen / Esc

Printer-friendly Version

Interactive Discussion



Variability and long-term trends of ocean acidification

C. Hauri et al.

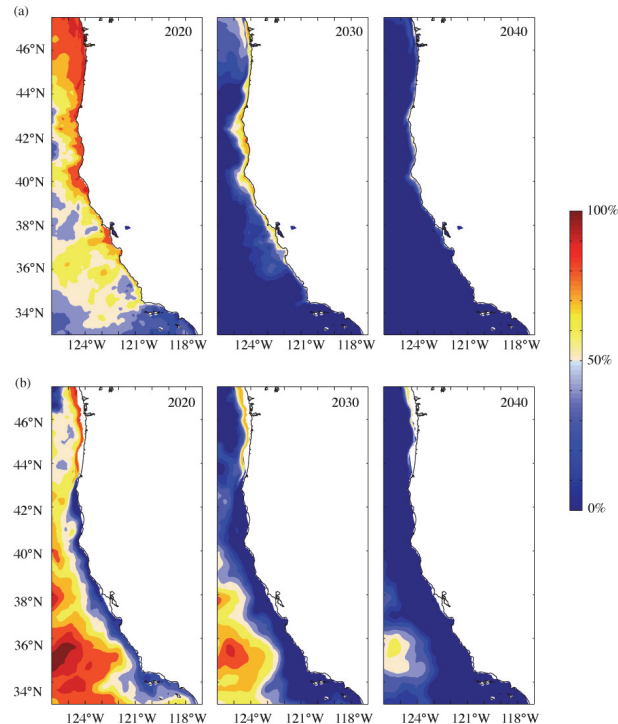


Fig. 14. The proportion of overlap in annual Ω_{arag} range (mean \pm (1 STD \times var_{cf})) of a ten year average at present for **(a)** the surface and **(b)** at 100 m depth, compared to ten year averages of every following decade until 2040. The years shown are the midpoints of the ten year average. The envelopes are adjusted with the correction factor var_{cf} (Sect. 2.4).

Title Page

Abstract

Introduction

Conclusions

References

Tables

Figures

◀

▶

◀

▶

Back

Close

Full Screen / Esc

Printer-friendly Version

Interactive Discussion



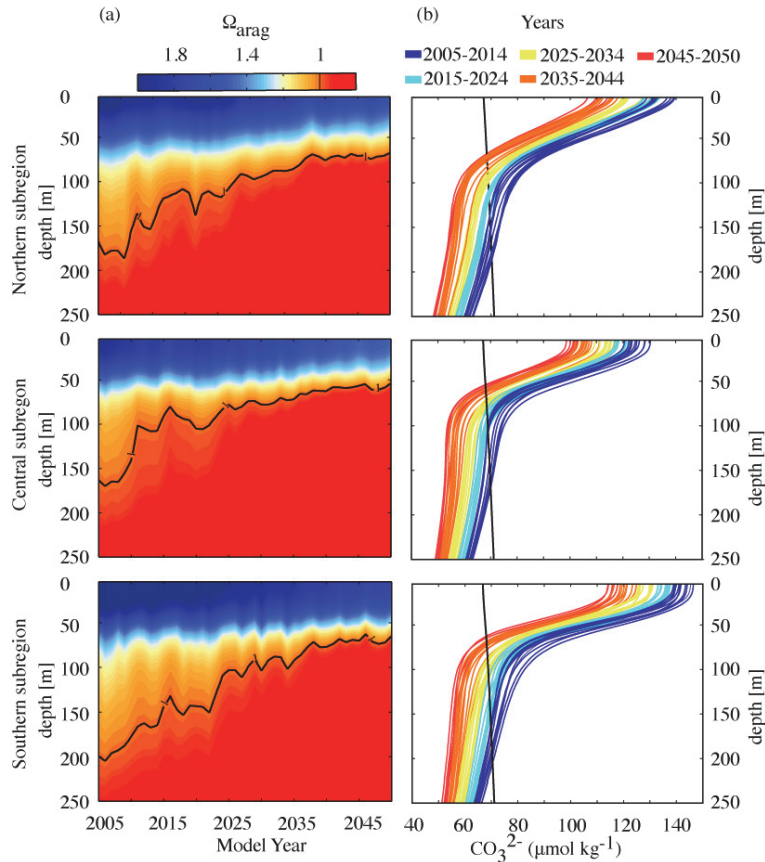


Fig. 15. (a) Evolution of the depth of aragonite saturation horizon as a function of time and depth. The depth of the saturation horizon is depicted as a black line. Panel **(b)** shows the expected shifts in the $[\text{CO}_3^{2-}]$ profiles for the years 2005–2050. The black line indicates the depth of the saturation horizon as a function of $[\text{CO}_3^{2-}]$ and depth.

Variability and long-term trends of ocean acidification

C. Hauri et al.

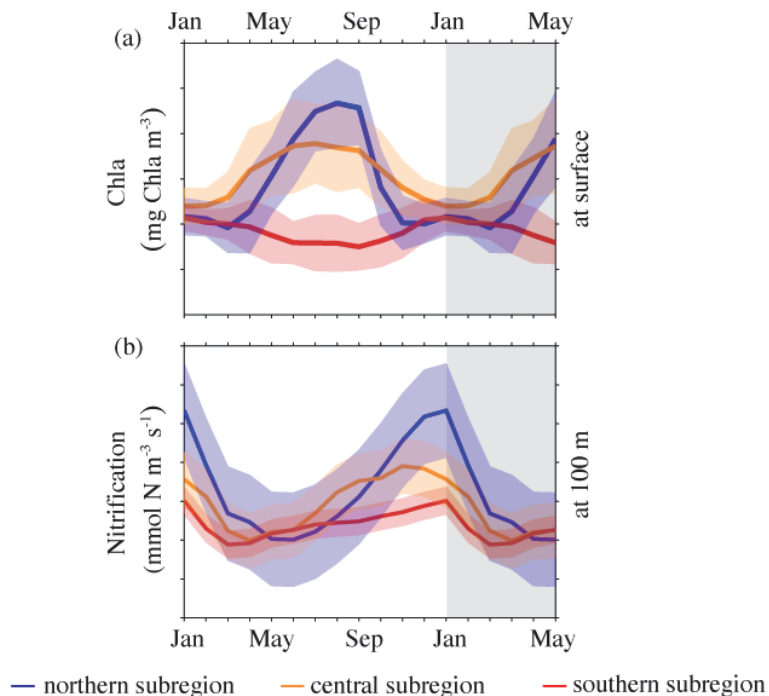


Fig. A1. Seasonal cycle of **(a)** surface chlorophyll *a* and **(b)** nitrification at 100 m, in the nearshore 50 km. The lines represent the mean and the shaded area the spatial variability (± 1 STD) for each month, for the northern (blue), central (orange) and southern (red) subregions. The shaded area depicts the first six months of the following annual cycle.

Title Page

Abstract

Introduction

Conclusions

References

Tables

Figures

◀

▶

◀

▶

Back

Close

Full Screen / Esc

Printer-friendly Version

Interactive Discussion



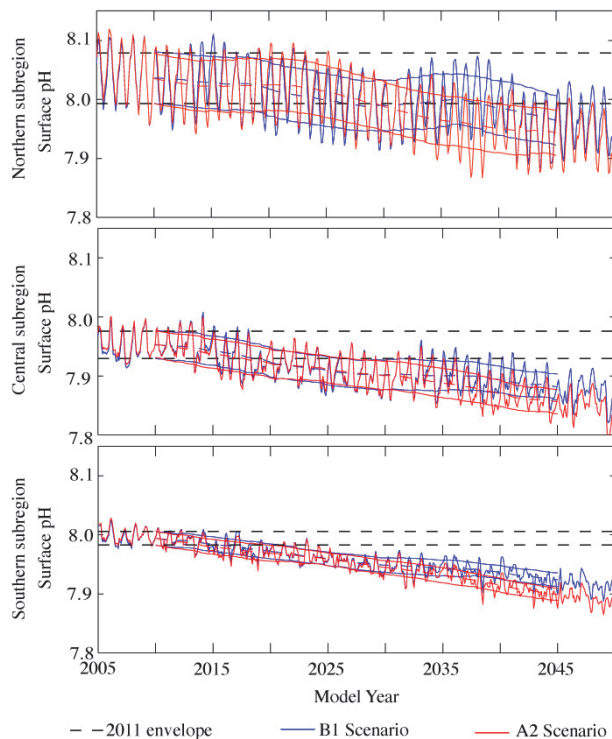


Fig. A2. Simulated timeseries of monthly mean surface pH for the two employed IPCC-SRES scenarios A2 (red) and B1 (blue), for the northern (top panel), central (center panel) and southern (bottom panel) subregions, with the 10-yr running average (dashed red and blue lines) of the mean for all grid cells of each subregion. The area between the solid lines defines the range of annual variability or envelope (mean \pm 1 STD) of pH for 2011 (black, \sim 395 ppm atmospheric $p\text{CO}_2$) and the transient simulations following the A2 (red) and B2 (blue) emissions scenarios. The results are based on simulations with the 15 km resolution set up.

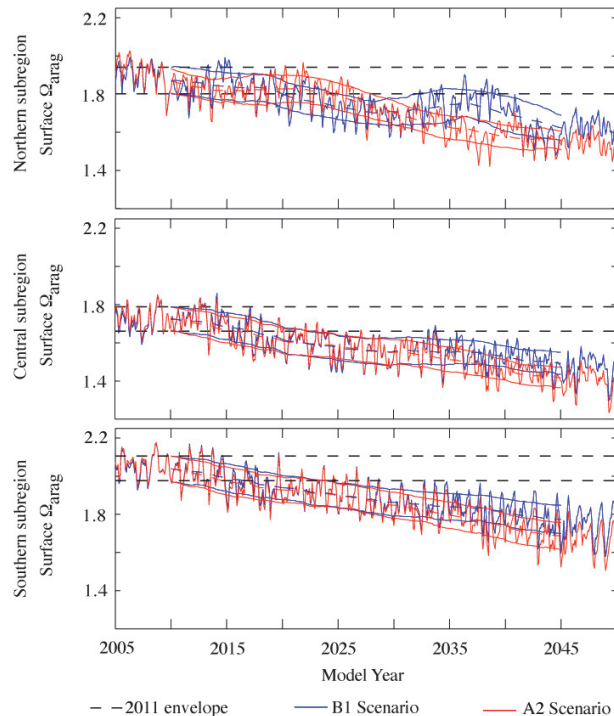


Fig. A3. Simulated timeseries of monthly mean surface Ω_{arag} for the two employed IPCC-SRES scenarios A2 (red) and B1 (blue), for the northern (top panel), central (center panel) and southern (bottom panel) subregions, with the 10-yr running average (dashed red and blue lines) of the mean for all grid cells of each subregion. The area between the solid lines defines the range of annual variability or envelope (mean \pm 1 STD) of Ω_{arag} for 2011 (black, \sim 395 ppm atmospheric $p\text{CO}_2$) and the transient simulations following the A2 (red) and B2 (blue) emissions scenarios. The results are based on simulations with the 15 km resolution set up.

Variability and long-term trends of ocean acidification

C. Hauri et al.

Title Page

Abstract Introduction

Conclusions References

Tables Figures

◀ ▶

◀ ▶

Back Close

Full Screen / Esc

Printer-friendly Version

Interactive Discussion

